Mathematics

http://www.aimspress.com/journal/Math

AIMS Mathematics, 11(7): 22316–22353.
DOI: 10.3934/math.2026903
Received: 26 May 2026
Revised: 22 June 2026
Accepted: 14 July 2026
Published: 27 July 2026

Research article

Incommensurate fractional epidemic dynamics with compartment-specific memory, treatment response, and physics-informed forecasting

Zied Elleuch[1], **Younes Brahim Oumedjber**[2], **Omar Kahouli**[3,*], **Adel Ouannas**[4], **Sulaiman Almohaimeed**[5,*], **Lilia El Amraoui**[6] **and Mohamed Ayari**[7,*]

[1] Computer Science Department, Applied College, University of Ha'il, 2440, Ha'il, Saudi Arabia

[2] Laboratory of Materials Science for Applications and the Environment (LaSMAE), Department of Sciences, Teacher Education College of Sétif–Messaoud Zeghar, P.O. Box 556, El Eulma, Sétif 19600, Algeria

[3] Department of Electronics Engineering, Applied College, University of Ha'il, Ha'il 2440, Saudi Arabia

[4] Department of Mathematics, Faculty of Science, Islamic University of Madinah, Madinah, Saudi Arabia

[5] Department of Electrical Engineering, College of Engineering, Qassim University, 52571, Saudi Arabia

[6] Department of Electrical Engineering, College of Engineering, Princess Nourah bint Abdulrahman University, P.O. Box 84428, Riyadh 11671, Saudi Arabia

[7] Department of Information Technology, Faculty of Computing and Information Technology, Northern Border University, Arar 91431, Saudi Arabia

* **Correspondence:** Email: a.kahouli@uoh.edu.sa, sulaiman.m@qu.edu.sa, mohamed.ayari@nbu.edu.sa.

Abstract: This paper develops an incommensurate fractional-order susceptible-exposed-symptomatic infectious-asymptomatic infectious-treated-recovered (SEIATR) model with compartment-specific Caputo memory. We establish local well-posedness, positivity, boundedness, biological feasibility, disease-free and endemic equilibria, and the basic reproduction number. Local stability is analyzed through the rational-order incommensurate Matignon criterion. A componentwise multi-order L1 scheme is then used for simulation, refinement, and sensitivity analysis. Finally, a physics-informed neural network is employed as a synthetic benchmark for hidden-state reconstruction, parameter and order identification, residual checking, and short-horizon forecasting. The results show that compartment-specific memory mainly affects peak timing, persistence, and treatment load, whereas epidemiological rates govern amplification and threshold behavior.

Keywords: incommensurate fractional order; Caputo derivative; SEIATR model; epidemic dynamics; L1 scheme; physics-informed neural network; forecasting
Mathematics Subject Classification:92D30, 34A08, 34D20, 65L05

1. Introduction

Compartmental epidemic models are standard tools for describing disease transmission, equilibria, threshold behavior, and intervention effects [1, 2]. Classical integer-order models are useful and interpretable, but they assume that the future evolution of each compartment depends only on the current state. This assumption can be restrictive when transmission, infection progression, treatment response, and recovery involve memory or persistence effects.

Fractional-order models provide a nonlocal way to describe such effects. The Caputo derivative is widely used in epidemic initial-value problems because it preserves classical initial conditions while introducing memory through convolution kernels [3–5]. Most fractional epidemic models are commensurate, meaning that the same order is imposed on all compartments. This simplification may be restrictive when susceptible, exposed, infectious, treated, and recovered populations evolve with different memory intensities.

Incommensurate and heterogeneous-memory fractional systems overcome this restriction by assigning different orders or memory structures to different state variables. Representative applications include COVID-19 dynamics and Hopfield neural networks [6, 7], Ebola and reaction–diffusion infection models [8, 9], and computer-virus propagation [10, 11]. A related COVID-19 SIR study is reported in [12]. Fractional epidemic studies on influenza, leishmaniasis, and related infection systems further motivate memory-based modelling [13–15]. Nonlinear-dynamics and numerical studies support threshold and sensitivity analyses [16–18].

From the analytical viewpoint, rational-order incommensurate fractional systems require stability tools that differ from the classical integer-order eigenvalue test. The local stability of equilibria is therefore formulated through the incommensurate Matignon criterion after rewriting the fractional orders with a common denominator [19, 20]. This distinction is important because the epidemic threshold and the fractional memory distribution play different roles: Epidemiological rates determine invasion, while the compartment-specific orders affect transient timing and persistence.

This paper develops an incommensurate fractional susceptible-exposed-symptomatic infectious-asymptomatic infectious-treated-recovered (SEIATR) model with Caputo orders $\nu_S, \nu_E, \nu_I, \nu_A, \nu_T$, and ν_R, assigned to the susceptible, exposed, symptomatic infectious, asymptomatic infectious, treated, and recovered compartments, respectively. The main contributions are the formulation of a compartment-specific memory SEIATR model, the proof of well-posedness and biological feasibility, the derivation of the disease-free and endemic equilibria, the computation of the basic reproduction number, the use of the rational-order incommensurate stability condition, and the implementation of a multi-order L1 numerical scheme.

The paper also includes a physics-informed computational learning component based on the general principle of physics-informed neural networks [21–23]. This component is used as a controlled synthetic benchmark, not as empirical surveillance calibration. Its purpose is to test whether hidden states, epidemiological parameters, and fractional orders can be reconstructed consistently with the governing multi-order SEIATR equations.

2. Preliminaries and multi-order SEIATR model

This section fixes the fractional notation and formulates the incommensurate SEIATR model. Let

$$X(t) = (S(t), E(t), I(t), A(t), T(t), R(t))^\top$$

denote the susceptible, exposed, symptomatic infectious, asymptomatic infectious, treated, and recovered populations. The total living population is

$$N(t) = S(t) + E(t) + I(t) + A(t) + T(t) + R(t).$$

2.1. Caputo multi-order setting

For $0 < \nu < 1$, the Caputo derivative of an absolutely continuous function x is defined by [3–5]

$$^{C}D_t^{\nu} x(t) = \frac{1}{\Gamma(1-\nu)} \int_0^t (t-s)^{-\nu} x'(s)\, ds, \qquad t > 0.$$

The equivalent Volterra form of

$$^{C}D_t^{\nu} x(t) = f(t, x(t)), \qquad x(0) = x_0,$$

is

$$x(t) = x_0 + \frac{1}{\Gamma(\nu)} \int_0^t (t-s)^{\nu-1} f(s, x(s))\, ds.$$

In the incommensurate case, different equations may have different orders. We use

$$\nu = (\nu_S, \nu_E, \nu_I, \nu_A, \nu_T, \nu_R), \qquad 0 < \nu_j < 1,$$

where $j \in \{S, E, I, A, T, R\}$. Thus,

$$^{C}D_t^{\nu_j} X_j(t) = F_j(X(t)),$$

or equivalently

$$X_j(t) = X_j(0) + \frac{1}{\Gamma(\nu_j)} \int_0^t (t-s)^{\nu_j-1} F_j(X(s))\, ds.$$

The commensurate case is recovered when

$$\nu_S = \nu_E = \nu_I = \nu_A = \nu_T = \nu_R.$$

In the present work, at least two entries of ν are different. If the orders are rational,

$$\nu_j = \frac{p_j}{q_j}, \qquad \gcd(p_j, q_j) = 1,$$

we set

$$M = \mathrm{lcm}(q_S, q_E, q_I, q_A, q_T, q_R),$$

which will be used in the local stability criterion for incommensurate systems [19].

2.2. Force of infection and model equations

Transmission is generated by $I(t)$ and $A(t)$. Symptomatic infectious individuals transmit with rate β, while asymptomatic individuals have relative infectivity θ_A, $0 < \theta_A \leq 1$. The standard-incidence force of infection is [1, 2]

$$\lambda(t) = \beta \frac{I(t) + \theta_A A(t)}{N(t)}.$$

The incommensurate fractional SEIATR system is

$$\begin{cases} {}^C D_t^{\nu_S} S = b - \lambda S - dS, \\ {}^C D_t^{\nu_E} E = \lambda S - (\sigma + d)E, \\ {}^C D_t^{\nu_I} I = p_s \sigma E - (\kappa + r_I + d)I, \\ {}^C D_t^{\nu_A} A = (1 - p_s)\sigma E - (r_A + d)A, \\ {}^C D_t^{\nu_T} T = \kappa I - (r_T + d)T, \\ {}^C D_t^{\nu_R} R = r_I I + r_A A + r_T T - dR. \end{cases} \tag{2.1}$$

Here b is the recruitment rate; d is the natural death rate; σ is the progression rate from exposure to infectiousness; p_s is the symptomatic fraction; κ is the treatment transfer rate; and $r_I, r_A,$ and r_T are the recovery rates from $I, A,$ and T, respectively. For compactness, define

$$K_E = \sigma + d, \qquad K_I = \kappa + r_I + d, \qquad K_A = r_A + d, \qquad K_T = r_T + d.$$

The parameters satisfy

$$b > 0, \quad d > 0, \quad \beta > 0, \quad \sigma > 0, \quad \kappa \geq 0, \quad r_I, r_A, r_T \geq 0,$$

and

$$0 < p_s < 1, \qquad 0 < \theta_A \leq 1.$$

The initial condition is

$$X(0) = X^0 = (S^0, E^0, I^0, A^0, T^0, R^0)^\top \in \mathbb{R}_+^6, \qquad N(0) > 0. \tag{2.2}$$

All rate coefficients are interpreted as effective rates after time normalization. Therefore, unless empirical calibration is performed, the simulation time axis is reported in normalized time units rather than calendar days.

3. Well-posedness of the multi-order model

This section proves that the proposed system is mathematically admissible. We establish local existence and uniqueness first; positivity and boundedness are treated separately because the force of infection is defined only when the total population is positive.

3.1. Existence and uniqueness of solutions

Let

$$X(t) = (S(t), E(t), I(t), A(t), T(t), R(t))^\top$$

and write system (2.1) in the componentwise form

$$ {}^C D_t^{\nu_j} X_j(t) = F_j(X(t)), \qquad j \in \{S, E, I, A, T, R\}.$$

Define

$$\mathcal{U} = \left\{X \in \mathbb{R}^6 : N(X) > 0\right\}, \qquad N(X) = S + E + I + A + T + R.$$

For $\eta > 0$, set

$$\mathcal{U}_\eta = \{X \in \mathcal{U} : N(X) > \eta\}.$$

On $\mathcal{U}_\eta$, the denominator in $\lambda(X)$ is bounded away from zero. Hence, the vector field $F = (F_S, F_E, F_I, F_A, F_T, F_R)^\top$ is continuously differentiable and locally Lipschitz.

Theorem 3.1. *Let $X^0 \in \mathcal{U}$. Then, the incommensurate fractional system* (2.1)*, together with the initial condition* (2.2)*, admits a unique local solution on some interval* $[0, T]$.

Proof. Choose $\eta > 0$ such that $X^0 \in \mathcal{U}_\eta$. Since F is locally Lipschitz on $\mathcal{U}_\eta$, there exist $r > 0$ and constants $M, L > 0$ such that, for all $X, Y \in B_r(X^0)$,

$$\|F(X)\|_\infty \le M, \qquad \|F(X) - F(Y)\|_\infty \le L\|X - Y\|_\infty.$$

For $T > 0$, define

$$\mathcal{X}_T = \left\{X \in C([0, T], \mathbb{R}^6) : \|X - X^0\|_\infty \le r\right\}.$$

Using the Volterra form of Caputo systems [4, 5], define the operator $\mathcal{T}$ componentwise by

$$(\mathcal{T}X)_j(t) = X_j^0 + \frac{1}{\Gamma(\nu_j)} \int_0^t (t - s)^{\nu_j - 1} F_j(X(s))\, ds.$$

Let

$$C_\nu = \max_{j\in\{S,E,I,A,T,R\}} \frac{1}{\Gamma(\nu_j + 1)}, \qquad \nu_{\min} = \min_{j\in\{S,E,I,A,T,R\}} \nu_j.$$

For $0 < T \le 1$, we have

$$\|\mathcal{T}X - X^0\|_\infty \le MC_\nu T^{\nu_{\min}}.$$

Thus, $\mathcal{T}(\mathcal{X}_T) \subset \mathcal{X}_T$ if

$$MC_\nu T^{\nu_{\min}} \le r.$$

Similarly,

$$\|\mathcal{T}X - \mathcal{T}Y\|_\infty \le LC_\nu T^{\nu_{\min}} \|X - Y\|_\infty.$$

Choosing $T > 0$ small enough so that

$$LC_\nu T^{\nu_{\min}} < 1,$$

the operator $\mathcal{T}$ is a contraction on $\mathcal{X}_T$. Banach's fixed-point theorem gives a unique fixed point of $\mathcal{T}$. This fixed point is the unique local solution of (2.1). □

The local solution can be extended as long as it remains bounded and the total population stays positive. These two properties are addressed in the next subsections.

3.2. Positivity of solutions

We prove that non-negative initial data generate non-negative trajectories. The argument uses the quasi-positivity of the vector field on the boundary of the non-negative cone [4, 24].

Theorem 3.2. *Let $X^0 \in \mathbb{R}^6_+$ with $N(0) > 0$. Then, every local solution of* (2.1) *satisfies*

$$S(t), E(t), I(t), A(t), T(t), R(t) \geq 0$$

for all t in its interval of existence.

Proof. Let

$$F(X) = (F_S, F_E, F_I, F_A, F_T, F_R)^\top$$

be the vector field of (2.1). On the boundary hyperplanes of $\mathbb{R}^6_+$, one has

$$F_S\big|_{S=0} = b \geq 0, \qquad F_E\big|_{E=0} = \lambda S \geq 0,$$

$$F_I\big|_{I=0} = p_s \sigma E \geq 0, \qquad F_A\big|_{A=0} = (1 - p_s)\sigma E \geq 0,$$

$$F_T\big|_{T=0} = \kappa I \geq 0, \qquad F_R\big|_{R=0} = r_I I + r_A A + r_T T \geq 0.$$

Therefore, the vector field is quasi-positive on $\mathbb{R}^6_+ \cap \mathcal{U}$.

Since F is locally Lipschitz on $\mathcal{U}_\eta$ for every $\eta > 0$, the invariance criterion for Caputo systems implies that $\mathbb{R}^6_+$ is positively invariant. Hence, a solution starting from $X^0 \in \mathbb{R}^6_+$ cannot leave the non-negative cone. □

The positivity result also guarantees that, as long as the solution exists and $N(t) > 0$, the force of infection $\lambda(t)$ remains epidemiologically meaningful.

3.3. Boundedness and biological feasibility

Since the model is incommensurate, the equations cannot be summed into a single Caputo equation for $N(t)$. We therefore use componentwise comparison estimates [4, 24].

Theorem 3.3. *Let $X^0 \in \mathbb{R}^6_+$ with $N(0) > 0$. Then, every non-negative solution of* (2.1) *is bounded and can be extended globally.*

Proof. For non-negative solutions and $0 < \theta_A \leq 1$,

$$0 \leq \frac{I + \theta_A A}{N} \leq 1, \qquad 0 \leq \lambda(t) \leq \beta.$$

Hence,

$${}^C D_t^{\gamma_S} S(t) \leq b - dS(t).$$

By the fractional comparison principle,

$$0 \leq S(t) \leq S_*, \qquad S_* = \max\left\{S^0, \frac{b}{d}\right\}.$$

Using this bound successively in the remaining equations gives

$$0 \le E(t) \le E_*, \qquad E_* = \max\left\{E^0, \frac{\beta S_*}{K_E}\right\},$$

$$0 \le I(t) \le I_*, \qquad I_* = \max\left\{I^0, \frac{p_s\sigma E_*}{K_I}\right\},$$

$$0 \le A(t) \le A_*, \qquad A_* = \max\left\{A^0, \frac{(1-p_s)\sigma E_*}{K_A}\right\},$$

$$0 \le T(t) \le T_*, \qquad T_* = \max\left\{T^0, \frac{\kappa I_*}{K_T}\right\},$$

and

$$0 \le R(t) \le R_*, \qquad R_* = \max\left\{R^0, \frac{r_I I_* + r_A A_* + r_T T_*}{d}\right\}.$$

Thus,

$$X(t) \in [0, S_*] \times [0, E_*] \times [0, I_*] \times [0, A_*] \times [0, T_*] \times [0, R_*]$$

on its interval of existence. Since the solution remains non-negative and bounded, the continuation theorem for Caputo systems implies global existence. □

Therefore, the biologically feasible region is

$$\Omega_* = [0, S_*] \times [0, E_*] \times [0, I_*] \times [0, A_*] \times [0, T_*] \times [0, R_*],$$

and every admissible trajectory remains in Ω_*.

4. Equilibria, reproduction number, and stability analysis

This section derives the disease-free and endemic equilibria, the basic reproduction number, and the local stability conditions. The stability part is written in the rational-order incommensurate form and is followed by a numerical verification for the baseline parameter set.

4.1. Disease-free equilibrium and basic reproduction number

At the disease-free equilibrium, the infected compartments vanish:

$$E = I = A = T = R = 0.$$

The susceptible equation gives

$$0 = b - dS.$$

Hence,

$$\mathcal{E}_0 = \left(\frac{b}{d}, 0, 0, 0, 0, 0\right). \tag{4.1}$$

Following the next-generation matrix approach [25], to compute the basic reproduction number, consider the infected vector

$$Y = (E, I, A)^\top.$$

The new-infection and transition terms are

$$\mathcal{F}(Y) = \begin{pmatrix} \lambda S \\ 0 \\ 0 \end{pmatrix}, \qquad \mathcal{V}(Y) = \begin{pmatrix} K_E E \\ -p_s \sigma E + K_I I \\ -(1-p_s)\sigma E + K_A A \end{pmatrix},$$

where

$$K_E = \sigma + d, \qquad K_I = \kappa + r_I + d, \qquad K_A = r_A + d.$$

At $\mathcal{E}_0$, $S_0 = N_0 = b/d$. Therefore,

$$F_0 = \begin{pmatrix} 0 & \beta & \beta\theta_A \\ 0 & 0 & 0 \\ 0 & 0 & 0 \end{pmatrix}, \qquad V_0 = \begin{pmatrix} K_E & 0 & 0 \\ -p_s\sigma & K_I & 0 \\ -(1-p_s)\sigma & 0 & K_A \end{pmatrix}.$$

A direct computation gives

$$F_0 V_0^{-1} = \begin{pmatrix} \dfrac{\beta\sigma}{K_E}\left(\dfrac{p_s}{K_I} + \dfrac{\theta_A(1-p_s)}{K_A}\right) & \dfrac{\beta}{K_I} & \dfrac{\beta\theta_A}{K_A} \\ 0 & 0 & 0 \\ 0 & 0 & 0 \end{pmatrix}.$$

Thus,

$$\mathcal{R}_0 = \frac{\beta\sigma}{\sigma + d}\left(\frac{p_s}{\kappa + r_I + d} + \frac{\theta_A(1-p_s)}{r_A + d}\right). \tag{4.2}$$

The fractional orders do not appear explicitly in $\mathcal{R}_0$, since the next-generation construction is based on the algebraic infection process at the disease-free equilibrium. They affect the transient dynamics and the local fractional stability condition through the characteristic equation.

4.2. Endemic equilibrium

Assume that $\mathcal{R}_0 > 1$. At an endemic equilibrium, $E^* > 0$, and the algebraic balance equations give

$$0 = b - \lambda^* S^* - dS^*, \qquad 0 = \lambda^* S^* - K_E E^*,$$

$$0 = p_s\sigma E^* - K_I I^*, \qquad 0 = (1-p_s)\sigma E^* - K_A A^*,$$

$$0 = \kappa I^* - K_T T^*, \qquad 0 = r_I I^* + r_A A^* + r_T T^* - dR^*.$$

Adding the six equilibrium equations gives $N^* = b/d$. Using $\lambda^* S^* = K_E E^*$ and (4.2), one obtains

$$S^* = \frac{b}{d\mathcal{R}_0}, \qquad E^* = \frac{b(\mathcal{R}_0 - 1)}{K_E \mathcal{R}_0}.$$

The remaining components are

$$I^* = \frac{p_s\sigma}{K_I}E^*, \qquad A^* = \frac{(1-p_s)\sigma}{K_A}E^*, \qquad T^* = \frac{\kappa}{K_T}I^*,$$

$$R^* = \frac{r_I I^* + r_A A^* + r_T T^*}{d}.$$

Therefore,

$$\mathcal{E}^* = (S^*, E^*, I^*, A^*, T^*, R^*). \tag{4.3}$$

Proposition 4.1. *The system* (2.1) *admits a unique biologically admissible endemic equilibrium $\mathcal{E}^*$ if and only if*

$$\mathcal{R}_0 > 1.$$

Proof. The above expressions uniquely determine all components of $\mathcal{E}^*$. Since $E^* > 0$ if and only if $\mathcal{R}_0 > 1$, and the remaining components are non-negative whenever $E^* > 0$, the endemic equilibrium is biologically admissible exactly when $\mathcal{R}_0 > 1$. □

4.3. Local stability of the incommensurate system

Let $\bar{X}$ be an equilibrium of (2.1), and let

$$J(\bar{X}) = \left[\frac{\partial F_i}{\partial X_j}(\bar{X})\right]_{i,j=1}^{6}$$

be the Jacobian matrix of the right-hand side. The linearized incommensurate system is

$${}^{C}D_t^{\nu_j} u_j(t) = \sum_{k=1}^{6} J_{jk}(\bar{X}) u_k(t), \qquad j \in \{S, E, I, A, T, R\}.$$

For rational orders $\nu_j = p_j/q_j$, with $\gcd(p_j, q_j) = 1$, define

$$M = \operatorname{lcm}(q_S, q_E, q_I, q_A, q_T, q_R).$$

The characteristic equation is

$$P_{\bar{X}}(z) = \det\left(\operatorname{diag}\left(z^{M\nu_S}, z^{M\nu_E}, z^{M\nu_I}, z^{M\nu_A}, z^{M\nu_T}, z^{M\nu_R}\right) - J(\bar{X})\right) = 0. \tag{4.4}$$

The equilibrium $\bar{X}$ is locally asymptotically stable if every root z of (4.4) satisfies

$$|\arg(z)| > \frac{\pi}{2M}. \tag{4.5}$$

This is the rational-order incommensurate Matignon criterion [19].

At the disease-free equilibrium,

$$J(\mathcal{E}_0) = \begin{pmatrix} -d & 0 & -\beta & -\beta\theta_A & 0 & 0 \\ 0 & -K_E & \beta & \beta\theta_A & 0 & 0 \\ 0 & p_s\sigma & -K_I & 0 & 0 & 0 \\ 0 & (1-p_s)\sigma & 0 & -K_A & 0 & 0 \\ 0 & 0 & \kappa & 0 & -K_T & 0 \\ 0 & 0 & r_I & r_A & r_T & -d \end{pmatrix}.$$

The infected part of the disease-free characteristic equation is

$$P_0(z) = (z^{M\nu_E} + K_E)(z^{M\nu_I} + K_I)(z^{M\nu_A} + K_A) - \beta p_s\sigma(z^{M\nu_A} + K_A) - \beta\theta_A(1-p_s)\sigma(z^{M\nu_I} + K_I). \tag{4.6}$$

Since

$$P_0(0) = K_E K_I K_A (1 - \mathcal{R}_0),$$

we have $P_0(0) < 0$ whenever $\mathcal{R}_0 > 1$. Moreover, $P_0(z) \to +\infty$ as $z \to +\infty$ on the positive real axis. Hence, by continuity, P_0 admits a positive real root. This root has argument zero and therefore violates (4.5). Thus, the disease-free equilibrium is locally unstable when $\mathcal{R}_0 > 1$.

For the endemic equilibrium, define

$$Q^* = I^* + \theta_A A^*, \qquad N^* = S^* + E^* + I^* + A^* + T^* + R^*.$$

Let

$$h_S = \beta \frac{Q^*(N^* - S^*)}{(N^*)^2}, \qquad h_E = -\beta \frac{S^* Q^*}{(N^*)^2}, \qquad h_I = \beta \frac{S^*(N^* - Q^*)}{(N^*)^2},$$
$$h_A = \beta \frac{S^*(\theta_A N^* - Q^*)}{(N^*)^2}, \qquad h_T = h_R = -\beta \frac{S^* Q^*}{(N^*)^2}.$$

Then,

$$J(\mathcal{E}^*) = \begin{pmatrix} -d - h_S & -h_E & -h_I & -h_A & -h_T & -h_R \\ h_S & h_E - K_E & h_I & h_A & h_T & h_R \\ 0 & p_s\sigma & -K_I & 0 & 0 & 0 \\ 0 & (1-p_s)\sigma & 0 & -K_A & 0 & 0 \\ 0 & 0 & \kappa & 0 & -K_T & 0 \\ 0 & 0 & r_I & r_A & r_T & -d \end{pmatrix}. \tag{4.7}$$

The roots of $P_{\mathcal{E}^*}(z)$ in (4.4) are computed numerically after substituting (4.7) into the rational-order characteristic determinant. For the baseline order vector, the exponents in (4.4) are

$$M\nu = (97,\ 92,\ 89,\ 86,\ 84,\ 94).$$

Thus, the endemic characteristic polynomial is

$$P_{\mathcal{E}^*}(z) = \det\left(\operatorname{diag}\left(z^{97}, z^{92}, z^{89}, z^{86}, z^{84}, z^{94}\right) - J(\mathcal{E}^*)\right), \tag{4.8}$$

and its degree is $97 + 92 + 89 + 86 + 84 + 94 = 542$. All roots of (4.8) are then computed numerically and tested against the angular condition (4.5).

4.4. Baseline numerical stability verification

For the baseline parameters used in the simulations,

$$b = 2200, \quad d = 0.002, \quad \beta = 0.50, \quad \theta_A = 0.70, \quad \sigma = 0.20, \quad p_s = 0.62, \quad \kappa = 0.07,$$
$$r_I = 0.08, \quad r_A = 0.06, \quad r_T = 0.05,$$

one obtains

$$\mathcal{R}_0 = 4.1432 > 1.$$

Thus, the disease-free equilibrium is unstable. The endemic equilibrium is

$$\mathcal{E}^* = (265495.081,\ 8262.425,\ 6740.399,\ 10128.134,\ 9073.614,\ 800300.347).$$

For the order vector $(0.97, 0.92, 0.89, 0.86, 0.84, 0.94)$, the rational representation gives $M = 100$ and

$$\frac{\pi}{2M} = 1.5708 \times 10^{-2}.$$

The numerical root test proceeds as follows. First, the endemic equilibrium $\mathcal{E}^*$ is substituted into the Jacobian matrix (4.7). Second, the rational-order characteristic determinant (4.8) is expanded as a polynomial in z. Third, all roots of this polynomial are computed, including multiplicities. Finally, the minimum angular distance from the positive real axis is evaluated as

$$\alpha_{\min} = \min_{P_{\mathcal{E}^*}(z)=0} |\arg(z)|.$$

The computed value $\alpha_{\min} = 1.86 \times 10^{-2}$ is strictly larger than $\pi/(2M) = 1.5708 \times 10^{-2}$. Hence, all characteristic roots lie outside the instability sector $|\arg(z)| \leq \pi/(2M)$, and the endemic equilibrium is locally asymptotically stable for the incommensurate baseline system.

As an additional check, the usual Jacobian eigenvalues at $\mathcal{E}^*$ are

$$-0.318943, \quad -0.097855, \quad -0.052000, \quad -0.002000, \quad -0.003744 \pm 0.019220i.$$

These integer-order eigenvalues are consistent with decay around the endemic equilibrium, but they do not replace the rational-order incommensurate root test. The decisive stability condition is the Matignon angular criterion verified in Tables 1 and 2.

Table 1. Baseline numerical verification of the incommensurate stability condition.

Equilibrium	Numerical result	Conclusion
$\mathcal{E}_0$	$\mathcal{R}_0 = 4.1432 > 1$; positive real root exists	Unstable
$\mathcal{E}^*$	$\min|\arg(z)| = 1.86 \times 10^{-2} > \pi/(2M)$	Locally asymptotically stable

Table 2. Numerical protocol for the incommensurate Matignon root test at $\mathcal{E}^*$.

Quantity	Value
Fractional-order vector	$(0.97, 0.92, 0.89, 0.86, 0.84, 0.94)$
Common denominator	$M = 100$
Polynomial exponents $M\nu_j$	$(97, 92, 89, 86, 84, 94)$
Degree of $P_{\mathcal{E}^*}(z)$	542
Stability threshold $\pi/(2M)$	1.5708×10^{-2}
Computed value $\min|\arg(z)|$	1.86×10^{-2}
Angular margin	2.892×10^{-3}

Remark 4.2. In the commensurate case $\nu_S = \nu_E = \nu_I = \nu_A = \nu_T = \nu_R = \nu$, criterion (4.5) reduces to

$$|\arg(\xi)| > \frac{\nu\pi}{2},$$

where ξ denotes an eigenvalue of the usual Jacobian matrix.

Remark 4.3. The threshold $\mathcal{R}_0$ determines invasion at the disease-free equilibrium, while (4.4) determines local stability for the rational-order incommensurate dynamics. Therefore, both the epidemiological threshold and the fractional-order distribution must be checked.

5. Multi-order numerical scheme and sensitivity analysis

This section introduces the numerical discretization used for the incommensurate SEIATR system. Since each compartment has its own fractional order, the memory weights are computed separately for each equation.

5.1. L1 discretization for different fractional orders

Let

$$t_n = n\Delta t, \qquad n = 0, 1, \ldots, N_T,$$

where $\Delta t > 0$ is the time step. For a scalar function $x(t)$, the L1 approximation of the Caputo derivative at t_n is given by [26]

$$^{C}D_t^{\nu} x(t_n) \approx \frac{1}{\Gamma(2-\nu)(\Delta t)^{\nu}} \sum_{k=0}^{n-1} a_k^{(\nu)} \left(x^{n-k} - x^{n-k-1} \right), \tag{5.1}$$

where

$$a_k^{(\nu)} = (k+1)^{1-\nu} - k^{1-\nu}.$$

For the multi-order SEIATR model, each compartment uses its own fractional order. Thus, for

$$X_j^n \approx X_j(t_n), \qquad j \in \{S, E, I, A, T, R\},$$

we define the componentwise L1 operator

$$\mathcal{D}_{\Delta t}^{\nu_j} X_j^n = \frac{1}{\Gamma(2-\nu_j)(\Delta t)^{\nu_j}} \sum_{k=0}^{n-1} a_{j,k} \left(X_j^{n-k} - X_j^{n-k-1} \right), \tag{5.2}$$

with

$$a_{j,k} = (k+1)^{1-\nu_j} - k^{1-\nu_j}.$$

Hence,

$$^{C}D_t^{\nu_j} X_j(t_n) \approx \mathcal{D}_{\Delta t}^{\nu_j} X_j^n. \tag{5.3}$$

Applying (5.2) to system (2.1) gives

$$\mathcal{D}_{\Delta t}^{\nu_j} X_j^n = F_j(X^n), \qquad j \in \{S, E, I, A, T, R\}. \tag{5.4}$$

In particular, the discrete force of infection is

$$\lambda^n = \beta \frac{I^n + \theta_A A^n}{N^n}, \qquad N^n = S^n + E^n + I^n + A^n + T^n + R^n.$$

The full discrete system is

$$\begin{cases} \mathcal{D}_{\Delta t}^{\nu_S} S^n = b - \lambda^n S^n - dS^n, \\ \mathcal{D}_{\Delta t}^{\nu_E} E^n = \lambda^n S^n - K_E E^n, \\ \mathcal{D}_{\Delta t}^{\nu_I} I^n = p_s \sigma E^n - K_I I^n, \\ \mathcal{D}_{\Delta t}^{\nu_A} A^n = (1-p_s)\sigma E^n - K_A A^n, \\ \mathcal{D}_{\Delta t}^{\nu_T} T^n = \kappa I^n - K_T T^n, \\ \mathcal{D}_{\Delta t}^{\nu_R} R^n = r_I I^n + r_A A^n + r_T T^n - dR^n. \end{cases} \tag{5.5}$$

The L1 approximation is componentwise: The weights $a_{j,k}$ are not shared by all equations. For sufficiently smooth scalar solutions, the nominal local accuracy of the L1 approximation in the j-th equation is $O((\Delta t)^{2-\nu_j})$. For the coupled multi-order system, the observed global accuracy is therefore governed by the least favorable componentwise order and by the regularity of the solution near the initial time.

Because (5.4) is evaluated at X^n, the time stepping is implicit and nonlinear through λ^n. Let

$$\tau_j = \Gamma(2-\nu_j)(\Delta t)^{\nu_j}, \qquad H_j^n = \sum_{k=1}^{n-1} a_{j,k}\left(X_j^{n-k} - X_j^{n-k-1}\right).$$

At each time level, the unknown vector X^n is obtained from

$$X_j^n = X_j^{n-1} - H_j^n + \tau_j F_j(X^n), \qquad j \in \{S, E, I, A, T, R\}. \tag{5.6}$$

In the reported simulations, (5.6) is solved by fixed-point iteration, initialized with $X^{n,0} = X^{n-1}$,

$$X_j^{n,m+1} = X_j^{n-1} - H_j^n + \tau_j F_j(X^{n,m}), \qquad m = 0, 1, 2, \ldots. \tag{5.7}$$

The iteration is stopped when

$$\frac{\|X^{n,m+1} - X^{n,m}\|_\infty}{1 + \|X^{n,m+1}\|_\infty} < 10^{-10}$$

or when the maximum number of iterations is reached. This explicitly specifies the nonlinear step used in the multi-order L1 implementation.

5.2. Time-step refinement and numerical accuracy

To verify that the reported trajectories are not artifacts of the selected time step, we performed a time-step refinement study for the multi-order L1 discretization. The baseline parameter set and the initial condition used in the simulations were kept fixed. The reference solution was computed with

$$\Delta t_{\mathrm{ref}} = 0.0625.$$

Coarser solutions obtained with

$$\Delta t = 1, \quad 0.5, \quad 0.25, \quad 0.125$$

were compared with the reference solution on the corresponding coarse time grids.

The comparison was based on the active epidemic burden

$$B(t) = E(t) + I(t) + A(t) + T(t). \tag{5.8}$$

For each time step Δt, the relative discrete error was computed as

$$\varepsilon_{\Delta t} = \frac{\left\|B_{\Delta t} - B_{\Delta t_{\mathrm{ref}}}\right\|_2}{\left\|B_{\Delta t_{\mathrm{ref}}}\right\|_2}, \tag{5.9}$$

where $B_{\Delta t_{\rm ref}}$ denotes the reference active burden restricted to the same time nodes as $B_{\Delta t}$. The observed refinement rate was then evaluated by

$$\rho_{\Delta t} = \frac{\log\left(\varepsilon_{\Delta t}/\varepsilon_{\Delta t/2}\right)}{\log(2)}. \tag{5.10}$$

Table 3 shows a systematic reduction of the relative error as Δt decreases. The observed rates are consistent with the expected refinement behavior of the L1 approximation for fractional-order problems, where the effective accuracy is influenced by the componentwise fractional orders, the coupling between compartments, the nonlinear force of infection, and the regularity of the solution near the initial time. Since the smallest order in the baseline vector is $\nu_T = 0.84$, the least favorable scalar L1 order is $2-\nu_T = 1.16$. The active-burden error may exhibit a higher observed refinement rate after the initial layer because it combines several compartments and is measured against a refined numerical reference. Therefore, the refinement study supports the numerical consistency of the baseline simulations and provides a direct check of the time-step dependence of the multi-order L1 implementation.

Table 3. Time-step refinement study for the multi-order L1 discretization. The error is computed for the active burden $B(t) = E(t) + I(t) + A(t) + T(t)$ relative to the reference solution obtained with $\Delta t_{\rm ref} = 0.0625$.

Δt	$\varepsilon_{\Delta t}$	Observed rate
1.0000	2.4914×10^{-2}	–
0.5000	1.0729×10^{-2}	1.215
0.2500	4.2564×10^{-3}	1.334
0.1250	1.3245×10^{-3}	1.684

5.3. Baseline multi-order epidemic dynamics

The baseline simulations were generated with the multi-order L1 scheme described in Section 5.1. No empirical surveillance data are used; the trajectories are synthetic model outputs used for numerical illustration and later learning benchmarks. Because the rates are effective normalized rates, the time variable is reported in normalized time units.

The baseline parameter values are

$$b = 2200, \quad d = 0.002, \quad \beta = 0.50, \quad \theta_A = 0.70, \quad \sigma = 0.20,$$

$$p_s = 0.62, \quad \kappa = 0.07, \quad r_I = 0.08, \quad r_A = 0.06, \quad r_T = 0.05.$$

The compartment-specific fractional orders are

$$(\nu_S, \nu_E, \nu_I, \nu_A, \nu_T, \nu_R) = (0.97, 0.92, 0.89, 0.86, 0.84, 0.94).$$

For comparison, the commensurate reference case uses

$$\nu_S = \nu_E = \nu_I = \nu_A = \nu_T = \nu_R = 0.93.$$

The initial condition is

$$X^0 = (870000,\ 3000,\ 1200,\ 800,\ 200,\ 124800)^\top.$$

The baseline computation uses

$$0 \le t \le 220, \qquad \Delta t = 1.$$

The variable t used in the simulations is a normalized computational time variable. Therefore, the interval $0 \le t \le 220$ and the step size $\Delta t = 1$ should not be interpreted as calibrated calendar days. All rate parameters are effective rates expressed with respect to this normalized time scale. This value of Δt is used for the baseline plots only; the numerical accuracy of the L1 discretization has been checked through the step-size refinement study in Table 3.

Figure 1 shows the baseline trajectories. Panels (a)–(d) report all compartments, the active compartments, the stacked active burden, and normalized active profiles.

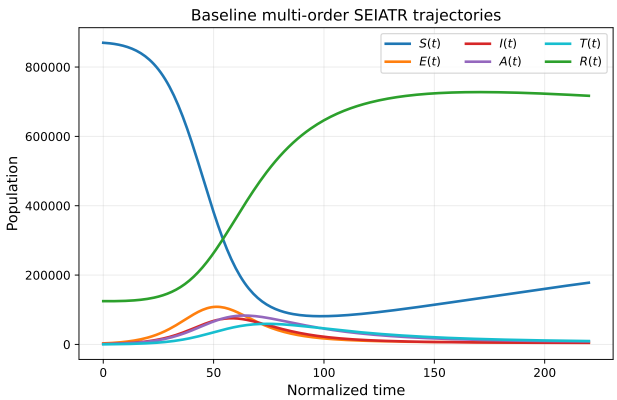

(a) All compartments.

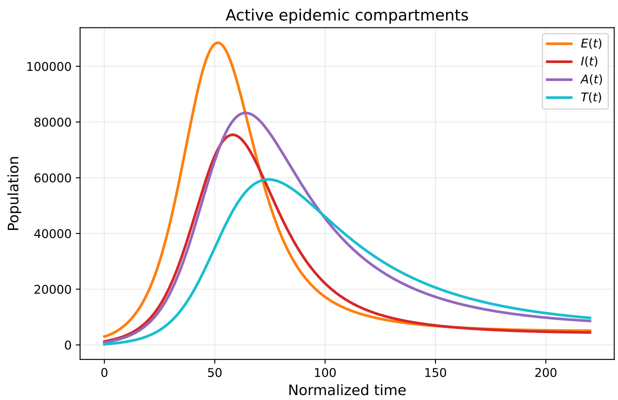

(b) Active compartments.

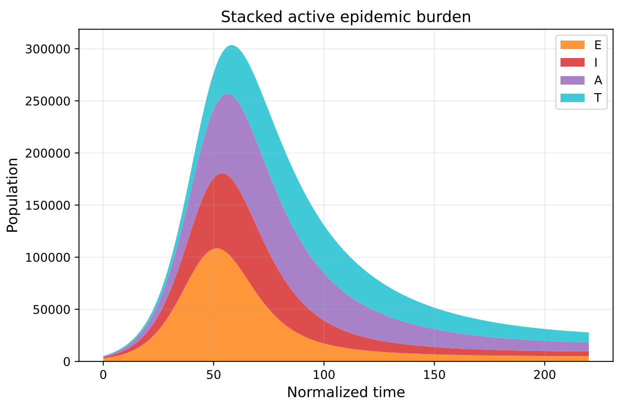

(c) Stacked active burden.

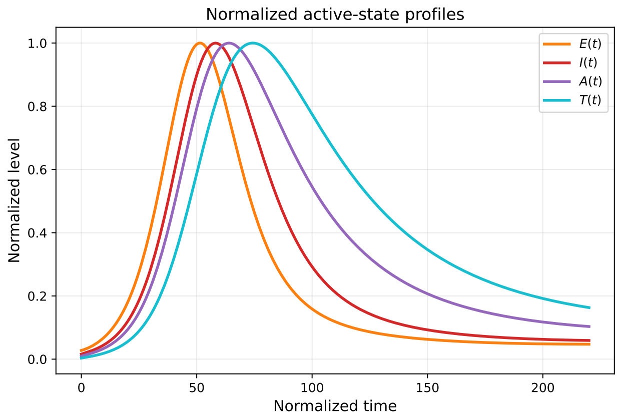

(d) Normalized active-state profiles.

Figure 1. Baseline multi-order SEIATR dynamics for the normalized parameter set. The horizontal axis represents the normalized computational time variable t. The incommensurate order vector is $(0.97, 0.92, 0.89, 0.86, 0.84, 0.94)$.

Figure 2 summarizes the active-burden structure. The commensurate and incommensurate curves differ mainly in timing and persistence, while the peak diagnostics show that the active classes do not peak simultaneously.

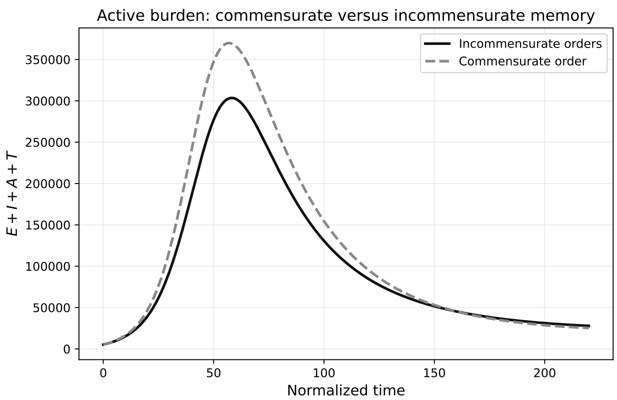

(a) Commensurate versus incommensurate active burden.

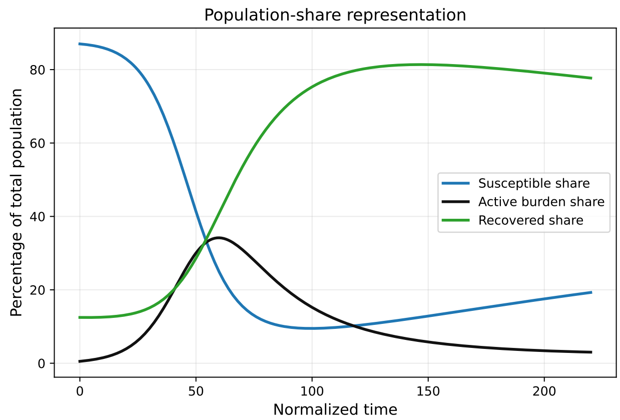

(b) Population shares.

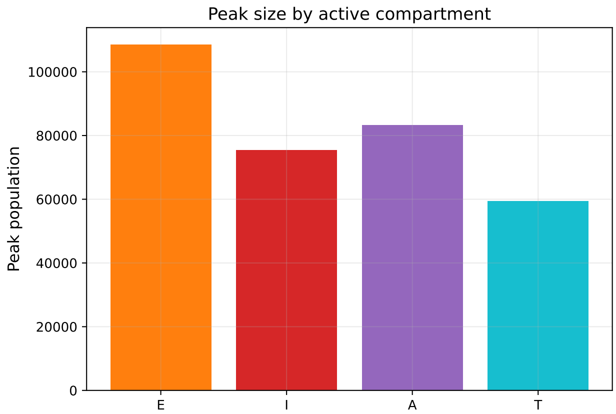

(c) Peak size by active compartment.

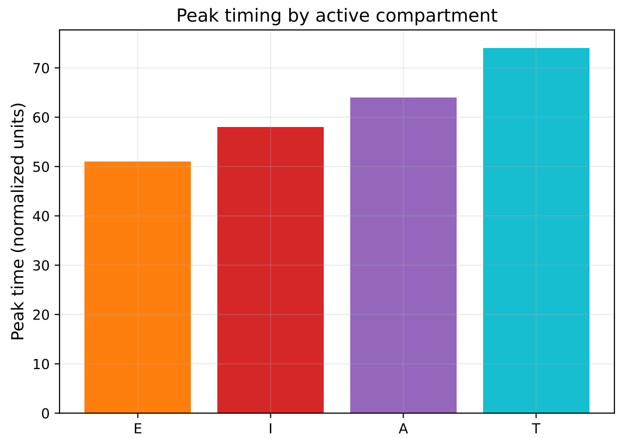

(d) Peak time by active compartment.

Figure 2. Baseline burden and peak diagnostics in normalized computational time. The commensurate reference uses the common order 0.93, while the incommensurate case uses $(0.97, 0.92, 0.89, 0.86, 0.84, 0.94)$.

The baseline computation shows that the active burden is distributed over E, I, A, and T, rather than being carried by the symptomatic class alone. The order-dependent comparison indicates that compartment-specific memory primarily modifies the timing and persistence of the active burden.

5.4. Sensitivity with respect to fractional orders and epidemiological parameters

We examine the influence of the compartment-specific fractional orders and selected epidemiological parameters on the epidemic dynamics. Unless otherwise stated, all simulations use the baseline parameter set and initial condition reported in Section 5.3. The tested fractional orders are

$$0.82, \quad 0.86, \quad 0.90, \quad 0.94, \quad 0.98.$$

The same normalized computational time scale is used throughout the sensitivity simulations. Therefore, peak times and time-dependent profiles are interpreted with respect to the normalized variable t, not as calibrated calendar days.

Figure 3 reports the most representative one-dimensional order sweeps. The symptomatic and asymptomatic curves show how the memory orders ν_I and ν_A modify the peak height and persistence of infection. The common-order sweep is retained as a reference to compare the incommensurate setting with the commensurate case.

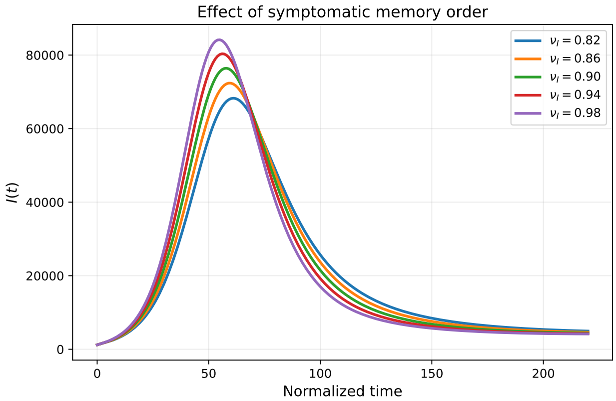

(a) Effect of ν_I on $I(t)$.

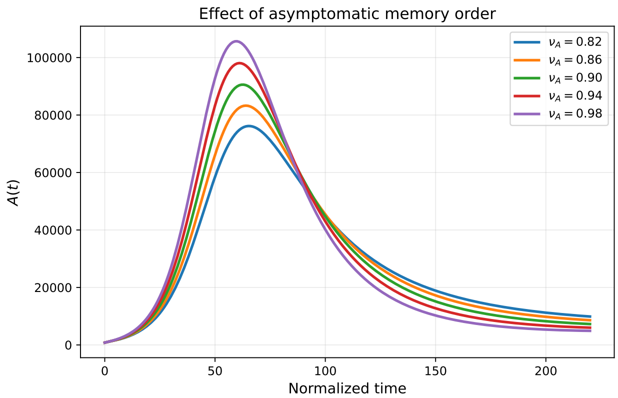

(b) Effect of ν_A on $A(t)$.

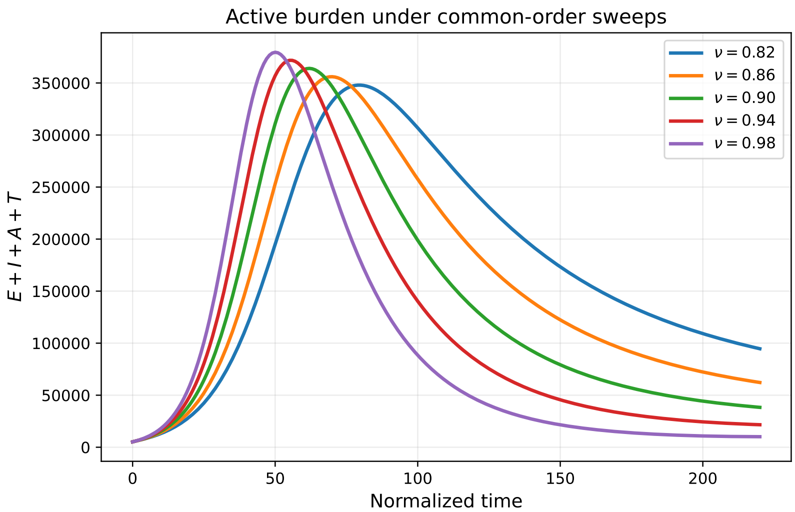

(c) Active burden under common-order sweeps.

Figure 3. Representative fractional-order sweeps in normalized computational time. Panels (a) and (b) vary one compartment-specific order at a time, while panel (c) varies a common order assigned to all compartments.

To avoid redundant visualizations, only the most informative heatmaps are retained. Figure 4 combines time-order, two-parameter, and threshold diagnostics. The first panel shows how ν_I affects the time profile of symptomatic infection. The second panel reports the combined influence of β and ν_I on the symptomatic peak. The third panel shows the cumulative treatment burden under changes in κ and ν_T. The last panel confirms that $\mathcal{R}_0$ is governed by epidemiological rates rather than directly by the fractional orders.

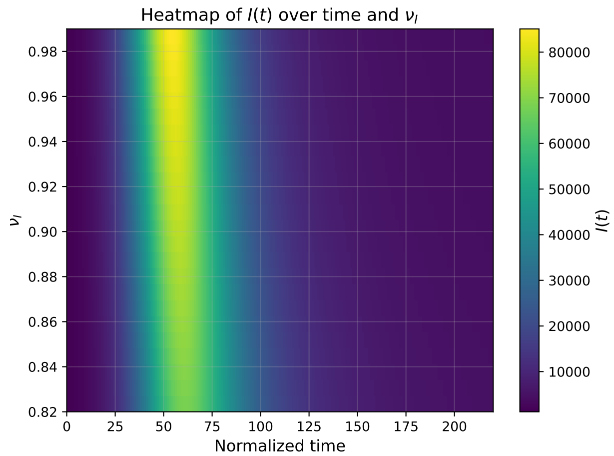

(a) Heatmap of $I(t)$ over time and ν_I.

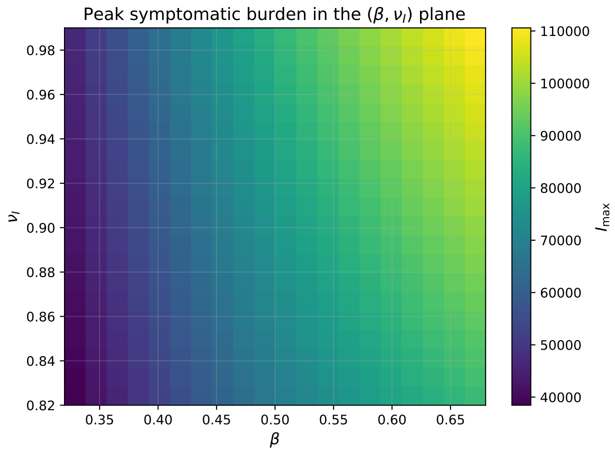

(b) Peak symptomatic burden in the (β, ν_I)-plane.

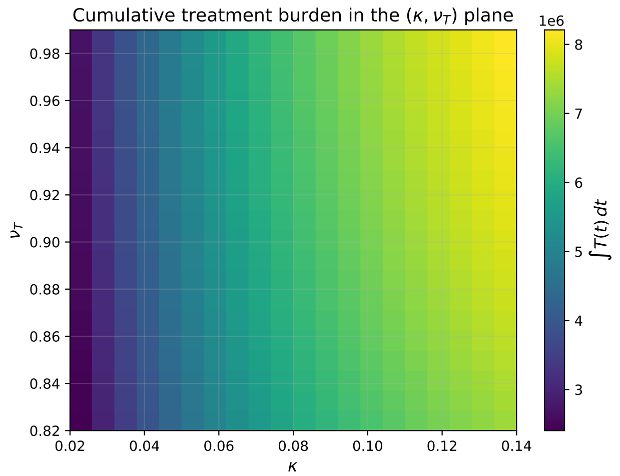

(c) Cumulative treatment burden in the (κ, ν_T)-plane.

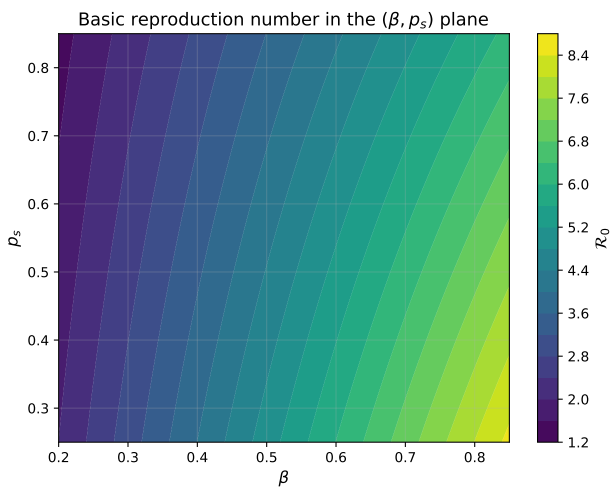

(d) $\mathcal{R}_0$ in the (β, p_s)-plane.

Figure 4. Selected sensitivity maps. Time-dependent panels use the normalized computational time variable t. The retained panels summarize the main effects of symptomatic memory, transmission intensity, treatment transfer, treatment memory, and the threshold quantity $\mathcal{R}_0$.

Finally, Figure 5 reports the one-at-a-time sensitivity of the symptomatic peak and the baseline fractional-order profile. The tornado plot uses a $\pm 15\%$ perturbation of the main epidemiological parameters around their baseline values. The order-profile panel displays the incommensurate memory structure used in the baseline simulation.

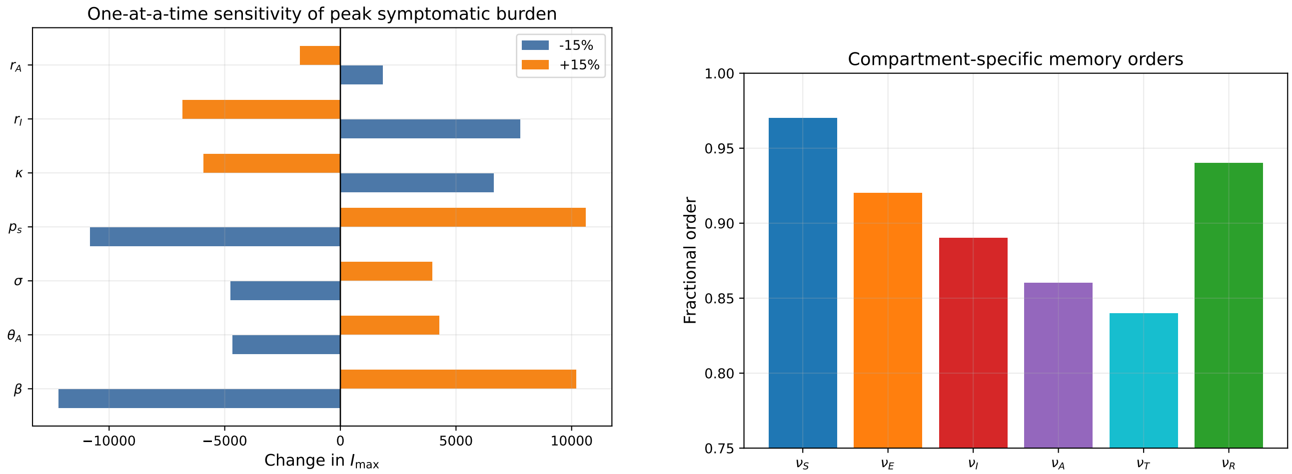

(a) One-at-a-time sensitivity of $I_{\max}$.

(b) Baseline fractional-order profile.

Figure 5. Reduced control and memory-order summary. The tornado plot uses ±15% perturbations of β, θ_A, σ, p_s, κ, r_I, and r_A. Peak-time diagnostics are interpreted in normalized computational time.

Overall, the reduced sensitivity analysis preserves the main conclusion: Epidemiological rates mainly control amplification and threshold behavior, while compartment-specific fractional orders regulate timing, broadening, and persistence of the epidemic wave. This supports the use of an incommensurate formulation without overloading the manuscript with redundant numerical figures.

6. Physics-informed learning, diagnostics, and forecasting

This section reports the physics-informed computational benchmark associated with the multi-order SEIATR model. The benchmark is fully synthetic: The reference trajectories are generated by the L1 discretization of (2.1), and no empirical surveillance data are used. Therefore, the results should be interpreted as a self-consistency and identifiability test of the proposed multi-order framework, not as a real-world forecasting validation.

The reference parameter set is the same as in Section 5:

$$b = 2200, \quad d = 0.002, \quad \beta = 0.50, \quad \theta_A = 0.70, \quad \sigma = 0.20, \quad p_s = 0.62, \quad \kappa = 0.07,$$

$$r_I = 0.08, \quad r_A = 0.06, \quad r_T = 0.05.$$

The reference fractional-order vector is

$$(\nu_S, \nu_E, \nu_I, \nu_A, \nu_T, \nu_R) = (0.97, 0.92, 0.89, 0.86, 0.84, 0.94),$$

with initial condition

$$X^0 = (870000,\ 3000,\ 1200,\ 800,\ 200,\ 124800)^\top.$$

The computational interval is $0 \le t \le 220$ in normalized time units with $\Delta t = 1$.

6.1. Synthetic observation signals and learning protocol

The observation channels are generated directly from the model states. The symptomatic-case signal and the healthcare-admission flow are defined by

$$C(t) = p_s \sigma E(t), \qquad H(t) = \kappa I(t).$$

Here, t denotes the normalized computational time variable used in Section 5. In this benchmark, the case and admission signals are sampled at consecutive normalized time steps; they are not calibrated calendar-day observations.

The chronological split is 70% for training, 15% for validation, and 15% for testing. The split is not shuffled, because the final task is short-horizon forecasting. In the baseline benchmark, no external stochastic noise is added to $C(t)$ and $H(t)$. Consequently, the very high reconstruction metrics reported below are expected and are interpreted as numerical consistency indicators rather than evidence of empirical predictive performance.

The neural approximation takes normalized time $\tau = t/220 \in [0, 1]$ as input and returns the normalized state vector

$$\widehat{X}(\tau) = (\widehat{S}, \widehat{E}, \widehat{I}, \widehat{A}, \widehat{T}, \widehat{R})^\top.$$

The implementation uses a fully connected feed-forward network with four hidden layers, 64 neurons per hidden layer, and hyperbolic tangent activation. State variables are normalized by their reference maximum values to avoid scale imbalance between the population compartments. The learnable quantities are β, κ, and the six fractional orders. Positivity of β and κ, and the constraints $0 < \nu_j < 1$, are enforced by smooth bounded transformations during training.

The complete implementation protocol is summarized in Table 4.

Table 4. PINN implementation details used in the computational benchmark.

Item	Specification
Input	Normalized time $\tau = t/220$
Outputs	Normalized $\widehat{S}, \widehat{E}, \widehat{I}, \widehat{A}, \widehat{T}, \widehat{R}$
Architecture	Fully connected feed-forward network
Hidden layers	4
Neurons per hidden layer	64
Activation function	tanh
Train–validation–test split	70%–15%–15%, chronological
Optimizer	Adam followed by L-BFGS refinement
Adam learning rate	10^{-3}
Stopping criterion	relative loss change below 10^{-8} or maximum iterations
Learned parameters	β, κ, $\nu_S, \nu_E, \nu_I, \nu_A, \nu_T, \nu_R$

The physics loss is constructed using the same L1 approximation as the numerical solver. Thus, the Caputo derivatives are not replaced by ordinary automatic differentiation. For each compartment, the discrete fractional residual is

$$\mathcal{R}_j^n = \mathcal{D}_{\Delta t}^{\widehat{\nu}_j} \widehat{X}_j^n - F_j(\widehat{X}^n; \widehat{\Theta}), \qquad j \in \{S, E, I, A, T, R\}, \tag{6.1}$$

where $\widehat{\Theta}$ contains the learned epidemiological parameters and fractional orders. The total loss is

$$\mathcal{L} = w_d \mathcal{L}_d + w_p \mathcal{L}_p + w_0 \mathcal{L}_0, \tag{6.2}$$

with data, physics, and initial-condition components defined by

$$\mathcal{L}_d = \frac{1}{N_o} \sum_{i=1}^{N_o} \left(\left| \widehat{C}_i - C_i \right|^2 + \left| \widehat{H}_i - H_i \right|^2 \right),$$

$$\mathcal{L}_p = \frac{1}{6N_T} \sum_{n=1}^{N_T} \sum_{j \in \{S,E,I,A,T,R\}} \left| \mathcal{R}_j^n \right|^2, \qquad \mathcal{L}_0 = \sum_{j \in \{S,E,I,A,T,R\}} \left| \widehat{X}_j^0 - X_j^0 \right|^2.$$

In the reported benchmark, the loss weights are set to $w_d = 1$, $w_p = 1$, and $w_0 = 10$, giving slightly stronger enforcement of the initial condition.

The chronological split and the two synthetic observation channels are shown in Figure 6.

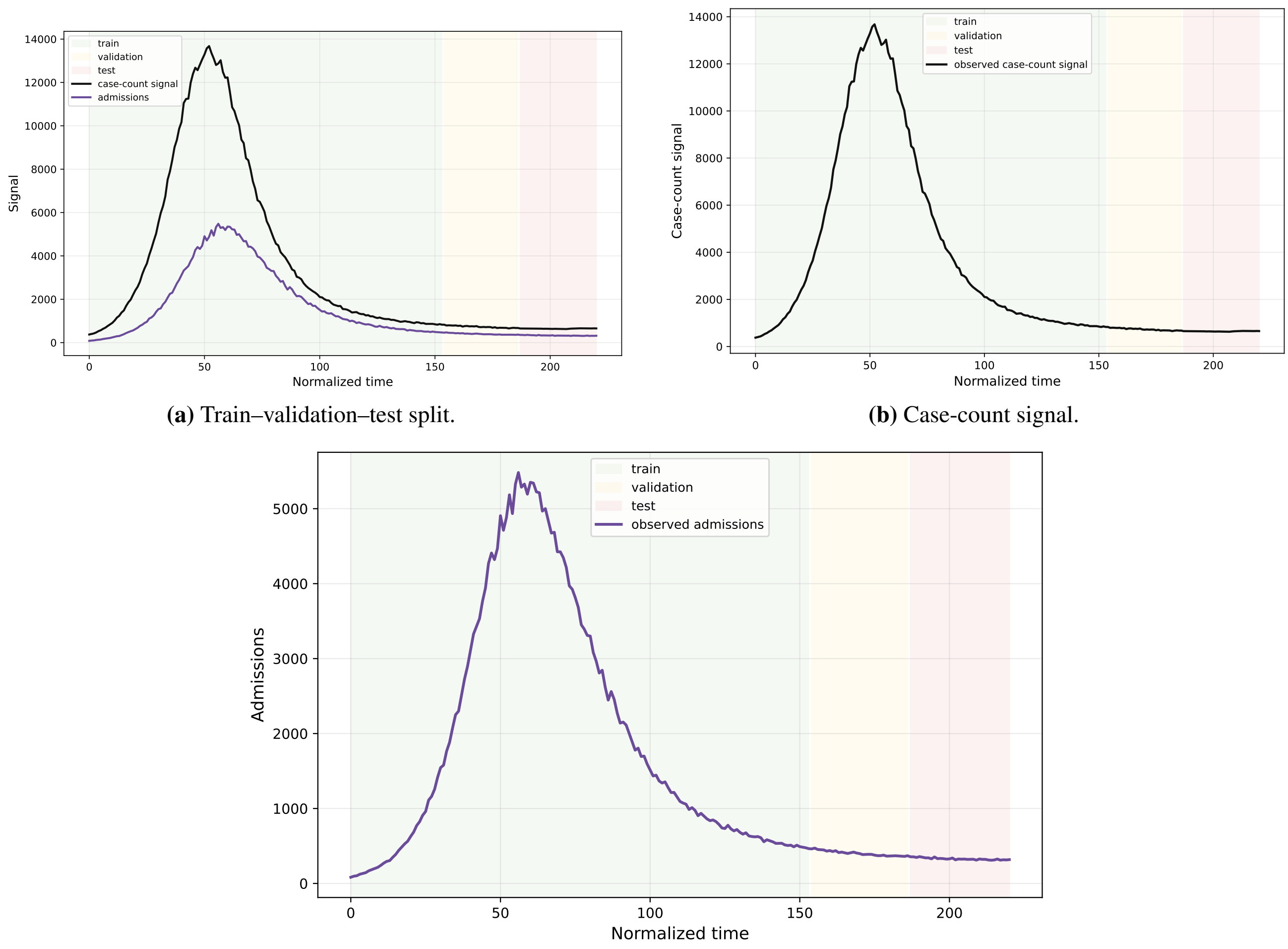

(a) Train–validation–test split.

(b) Case-count signal.

(c) Healthcare-admission signal.

Figure 6. Synthetic observation signals used in the physics-informed benchmark under the normalized computational time scale.

6.2. State reconstruction and observation fitting

The first diagnostic compares the reconstructed hidden active states with the L1 reference trajectories. The learning task is not limited to fitting $C(t)$ and $H(t)$, because the hidden variables $E(t)$, $I(t)$, $A(t)$, and $T(t)$ are constrained by the multi-order SEIATR residual. The compartmentwise reconstructions and the joint observation fits are presented in Figures 7 and 8, respectively.

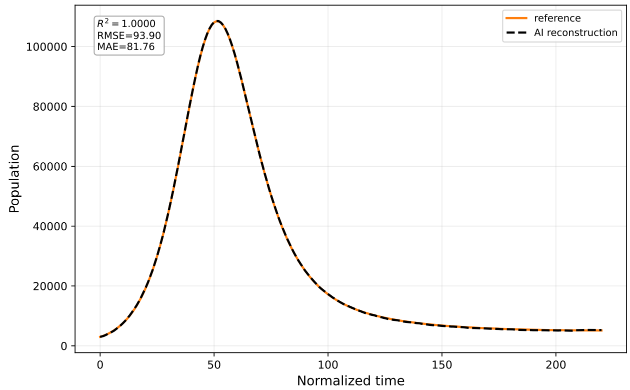

(a) Reconstruction of $E(t)$.

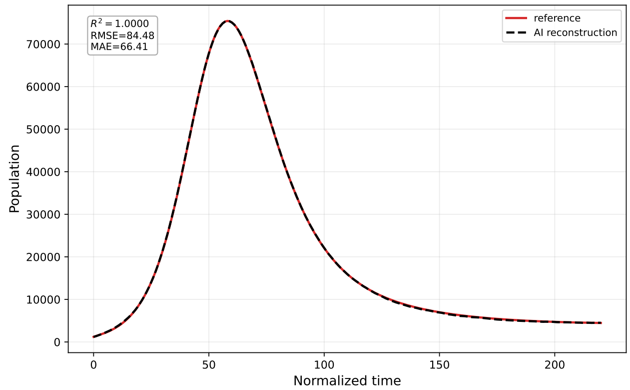

(b) Reconstruction of $I(t)$.

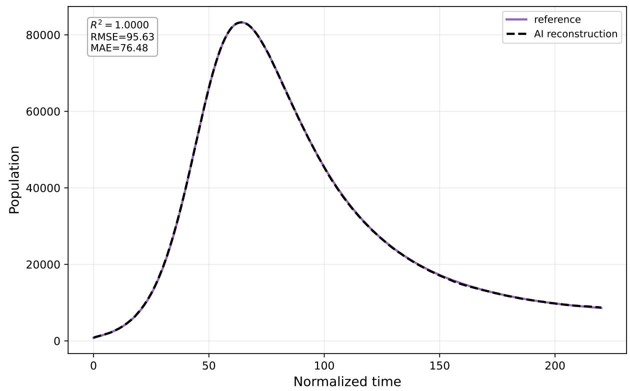

(c) Reconstruction of $A(t)$.

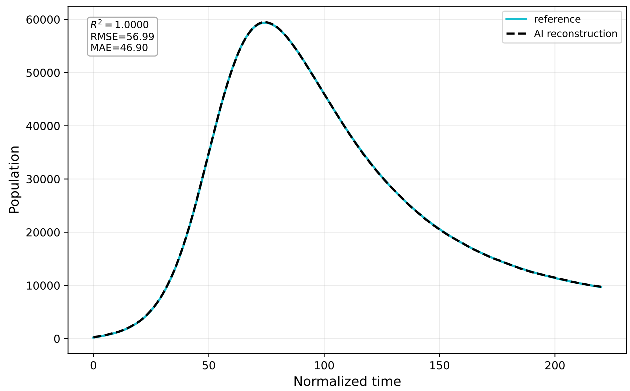

(d) Reconstruction of $T(t)$.

Figure 7. Reconstruction of hidden active states from the synthetic observation channels and the multi-order physics constraint under the normalized computational time scale.

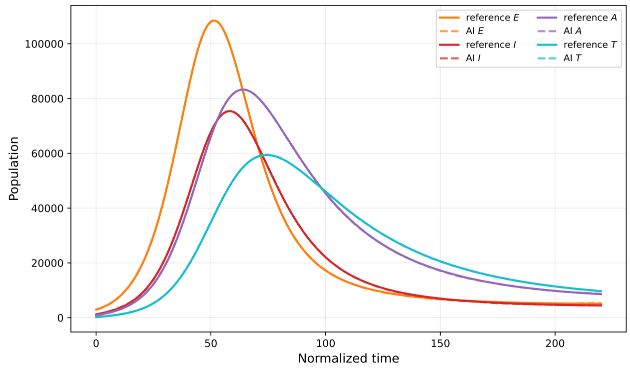

(a) Joint active-state reconstruction.

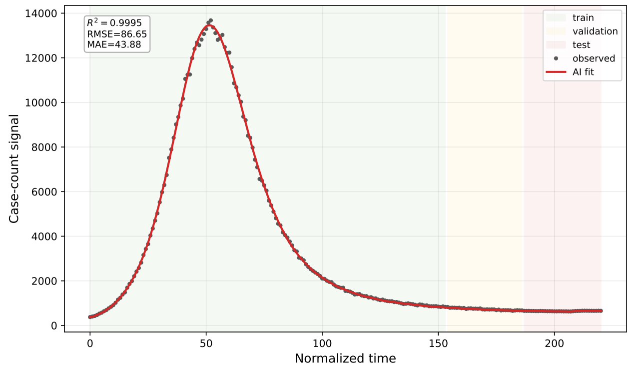

(b) Case-count reconstruction.

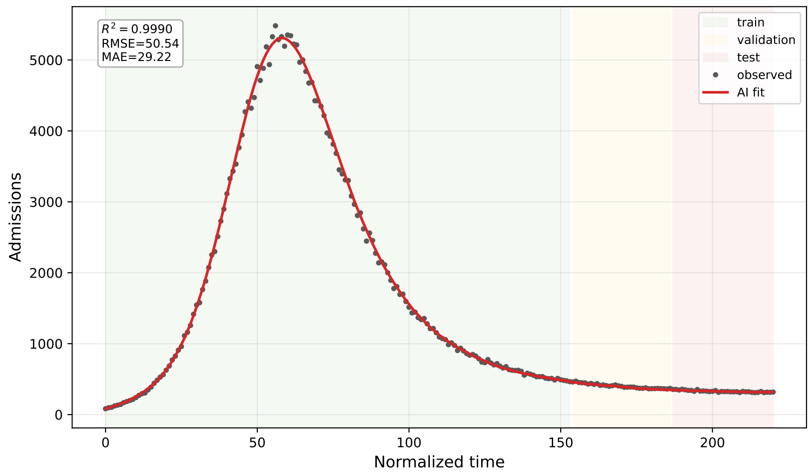

(c) Admission reconstruction.

Figure 8. Joint active-state reconstruction and fitting of the two synthetic observation channels under the normalized computational time scale.

The reconstruction metrics are summarized once in Table 5. This avoids repeating the same numerical values in several subsections.

Table 5. Reconstruction metrics for the hidden states and observation channels.

Quantity	R^2	RMSE	MAE	MAPE
$E(t)$	0.999991	93.90	–	–
$I(t)$	0.999986	84.48	–	–
$A(t)$	0.999985	95.63	–	–
$T(t)$	0.999990	56.99	–	–
Case-count signal $C(t)$	0.999500	86.65	43.88	1.28%
Admissions $H(t)$	0.998960	50.54	29.22	2.06%

Because the benchmark is synthetic and noise-free, the near-perfect values in Table 5 are not unexpected. They show that the implemented learning framework can recover the internally generated multi-order trajectories, but they do not by themselves demonstrate performance on noisy real surveillance data.

6.3. Noisy synthetic-observation stress test

To quantify the sensitivity of the observation-fit metrics to measurement imperfections, we performed an additional controlled noise-injection test on the two observable channels. For a relative noise level η, the perturbed case-count and admission signals were generated by

$$C_\eta(t_n) = \max\left\{C(t_n)\left(1+\eta\xi_n^C\right), 0\right\}, \qquad H_\eta(t_n) = \max\left\{H(t_n)\left(1+\eta\xi_n^H\right), 0\right\}, \tag{6.3}$$

where ξ_n^C and ξ_n^H are independent zero-mean unit-variance Gaussian variables generated with a fixed seed. The tested noise levels are

$$\eta = 0\%, \quad 1\%, \quad 3\%, \quad 5\%.$$

The reconstructed trajectories and the corresponding observation functions were then evaluated against C_η and H_η. This diagnostic does not represent empirical surveillance calibration. It directly tests how the reported observation-level metrics degrade when the synthetic observation channels are perturbed.

Table 6 shows the expected monotone degradation of RMSE and MAPE as the perturbation level increases. The coefficients of determination remain above 0.994 at the 5% noise level for both observation channels, indicating that the reconstructed signals retain the dominant synthetic dynamics under moderate observation noise. These results are still limited to controlled synthetic perturbations; they should not be interpreted as validation under reporting delays, missing data, changing testing policies, or model misspecification.

Table 6. Noise-injection stress test for the synthetic observation channels. Metrics are computed between the reconstructed observation functions and the perturbed signals C_η and H_η.

Noise level	RMSE(C_η)	MAPE(C_η)	R_C^2	RMSE(H_η)	MAPE(H_η)	R_H^2
0%	11.64	0.93%	0.999991	14.42	0.96%	0.999915
1%	49.17	1.21%	0.999839	28.39	1.19%	0.999671
3%	135.62	2.60%	0.998774	61.89	2.52%	0.998431
5%	233.00	3.96%	0.996412	113.88	4.26%	0.994612

6.4. Training convergence and parameter identification

The learning process is monitored through the data loss, physics-residual loss, initial-condition loss, and validation loss. Figure 9 shows stable convergence without visible separation between training and validation behavior.

The transmission rate β, the treatment rate κ, and the six fractional orders are treated as learnable quantities. Their convergence traces are reported in Figure 10.

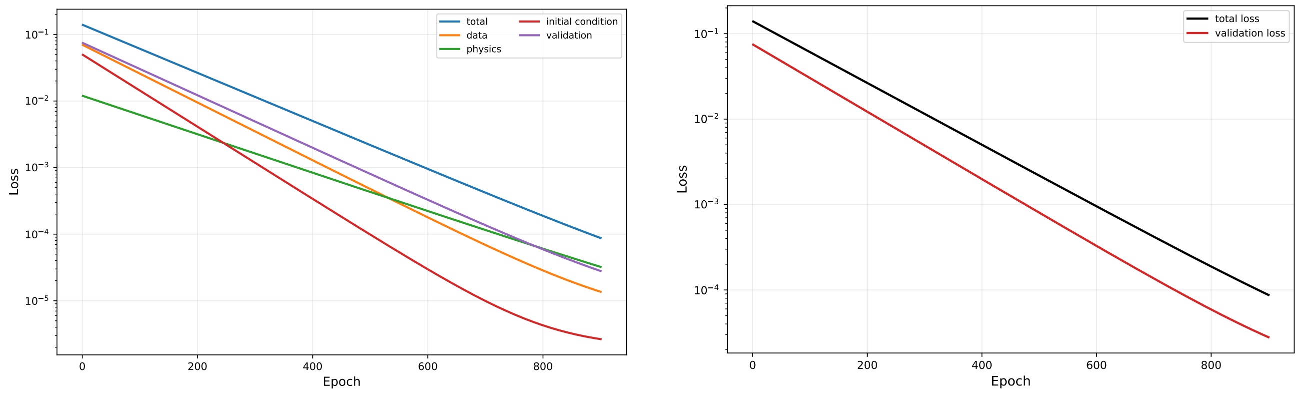

(a) Loss components. **(b)** Total and validation loss.

Figure 9. Training convergence of the physics-informed learning framework.

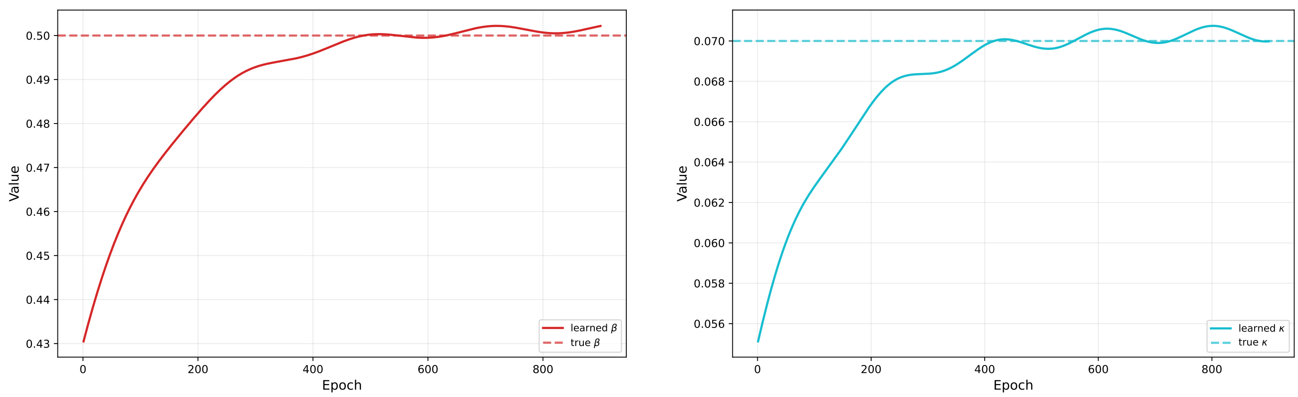

(a) Trace of β. **(b)** Trace of κ.

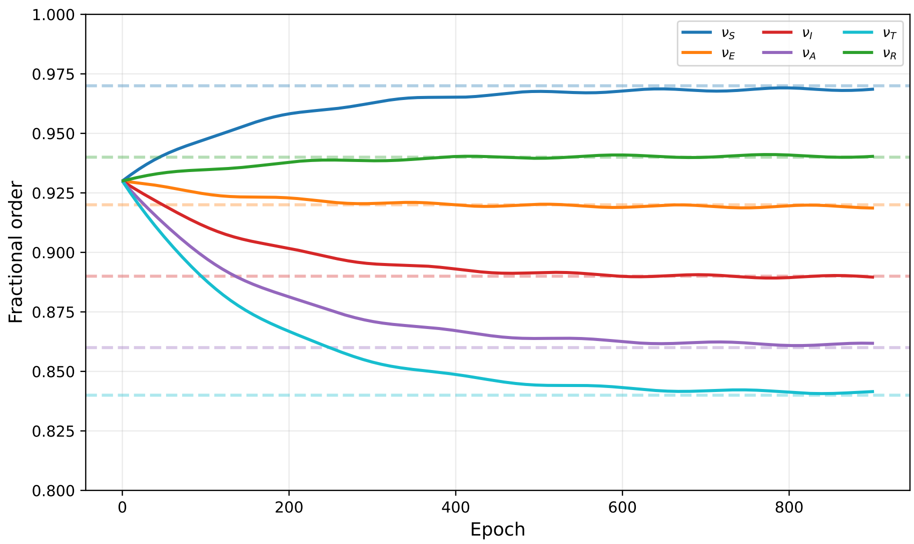

(c) Traces of the compartment-specific orders.

Figure 10. Convergence traces of the learned epidemiological parameters and fractional orders.

The identified values are

$$\widehat{\beta} = 0.5018, \qquad \widehat{\kappa} = 0.0704,$$

compared with $\beta = 0.5000$ and $\kappa = 0.0700$. The learned fractional-order vector is

$$(\widehat{\nu_S}, \widehat{\nu_E}, \widehat{\nu_I}, \widehat{\nu_A}, \widehat{\nu_T}, \widehat{\nu_R}) = (0.9688, 0.9192, 0.8895, 0.8610, 0.8408, 0.9406),$$

while the reference vector is (0.9700, 0.9200, 0.8900, 0.8600, 0.8400, 0.9400). The absolute errors are below 1.2×10^{-3}, which indicates accurate parameter recovery in the controlled benchmark.

6.5. *Parity and residual diagnostics*

Parity plots for the hidden states and observable signals are shown in Figures 11 and 12, respectively, while the metrics are reported in Table 5. This avoids the repetition of identical metric values.

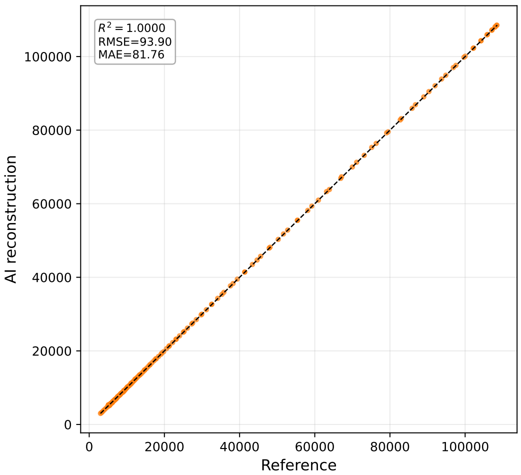

(a) Parity plot for $E(t)$.

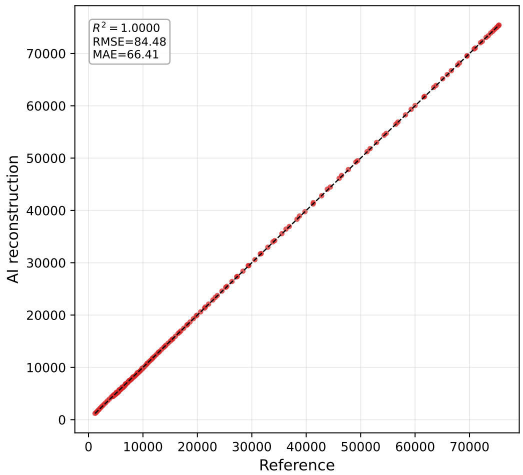

(b) Parity plot for $I(t)$.

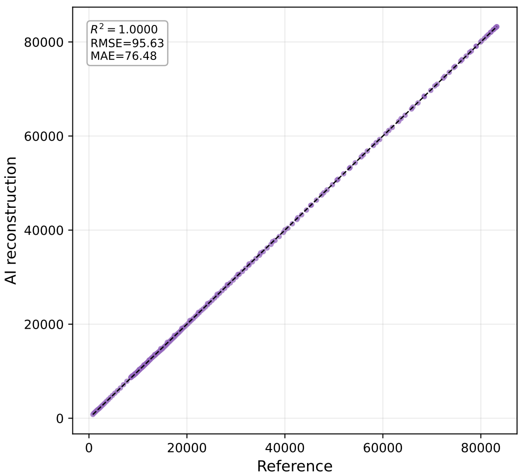

(c) Parity plot for $A(t)$.

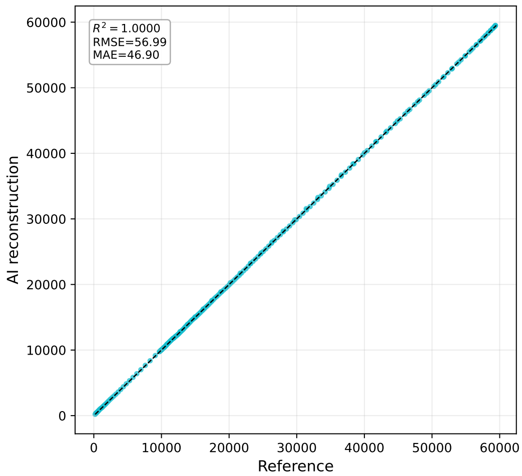

(d) Parity plot for $T(t)$.

Figure 11. Parity diagnostics for the reconstructed hidden epidemic states.

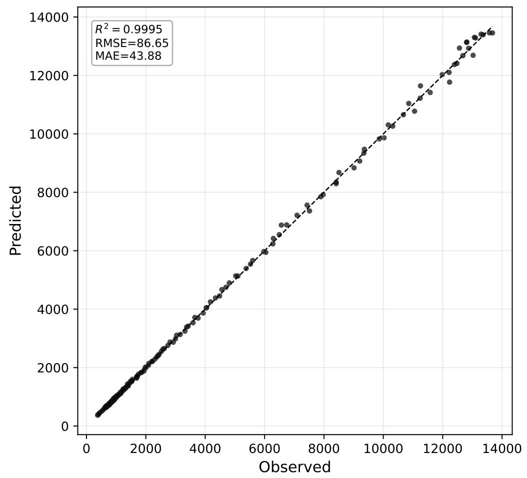

(a) Parity plot for the case-count signal.

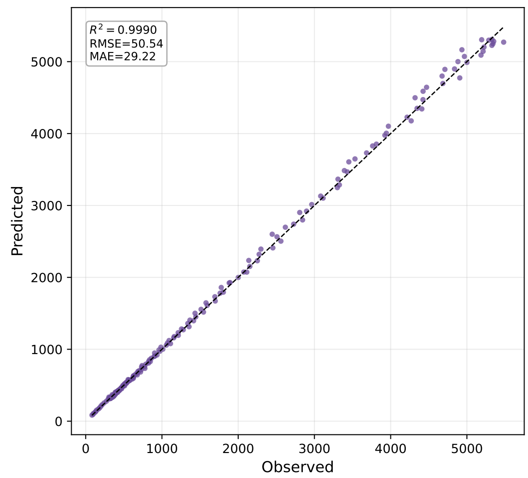

(b) Parity plot for admissions.

Figure 12. Parity diagnostics for the observable benchmark signals.

For a reconstructed quantity $Y(t)$, the residual is defined as

$$e_Y(t_i) = \widehat{Y}(t_i) - Y(t_i).$$

Figures 13 and 14 show the residuals over time. The errors remain small relative to the corresponding signal magnitudes and do not show a persistent drift over the benchmark interval.

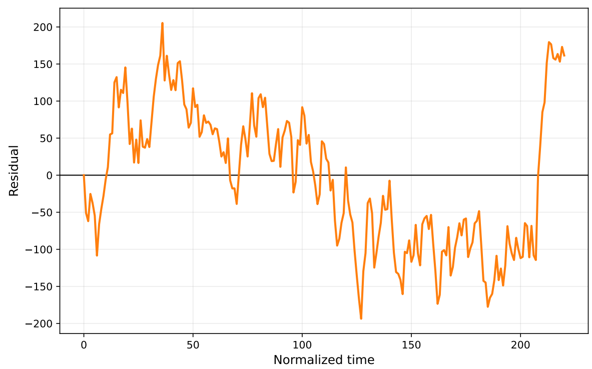

(a) Residuals for $E(t)$.

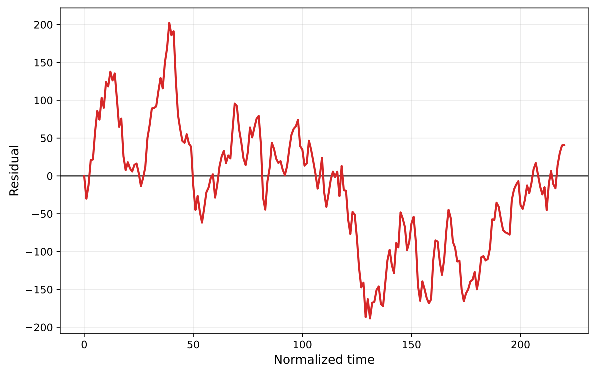

(b) Residuals for $I(t)$.

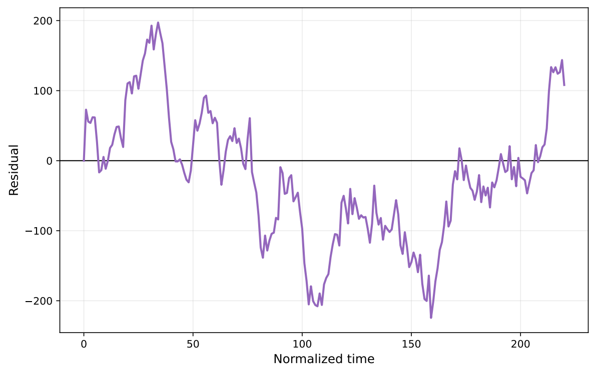

(c) Residuals for $A(t)$.

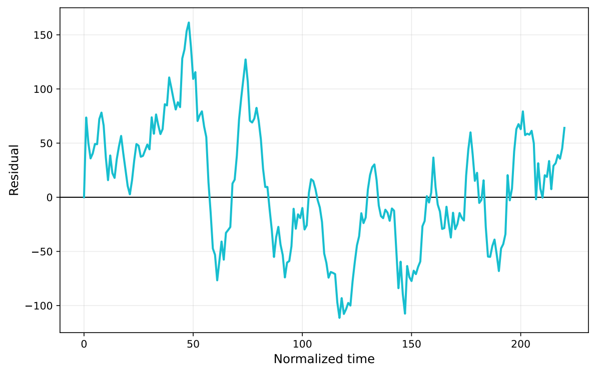

(d) Residuals for $T(t)$.

Figure 13. Time evolution of reconstruction residuals for the hidden active states.

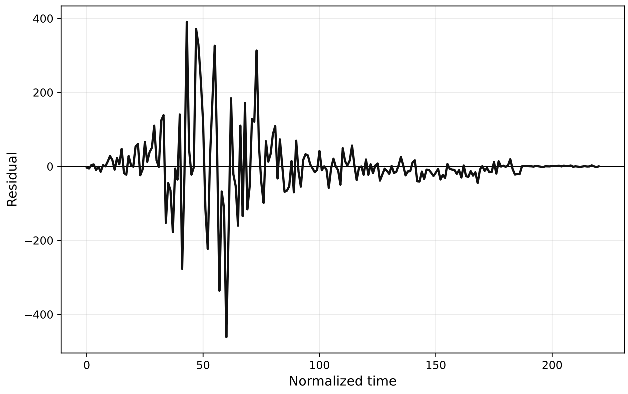

(a) Case-count residuals.

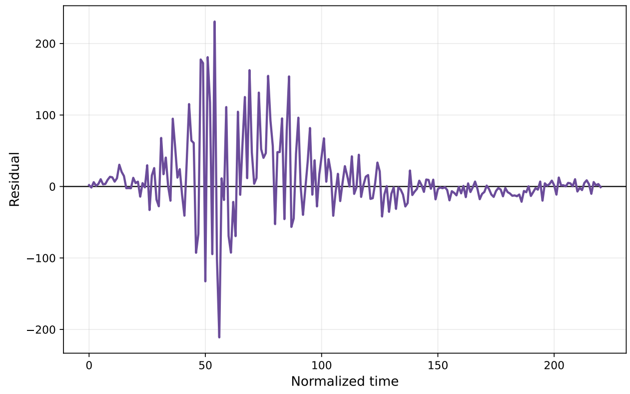

(b) Admission residuals.

Figure 14. Residuals of the synthetic observation channels under the normalized computational time scale.

The corresponding residual distributions are summarized in Figures 15 and 16.

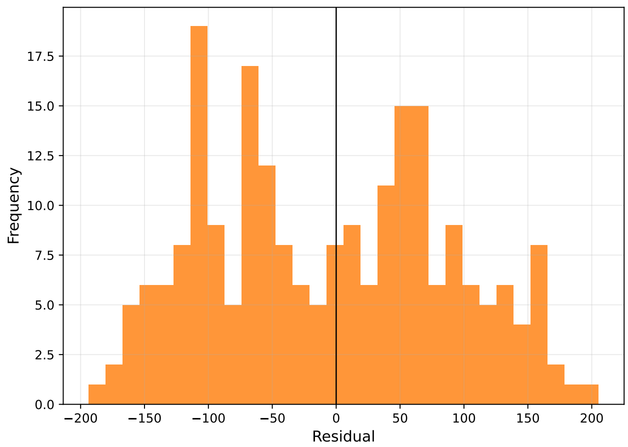

(a) Residual distribution for $E(t)$.

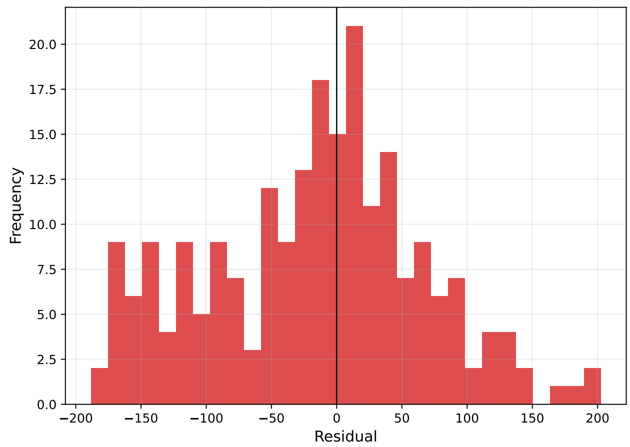

(b) Residual distribution for $I(t)$.

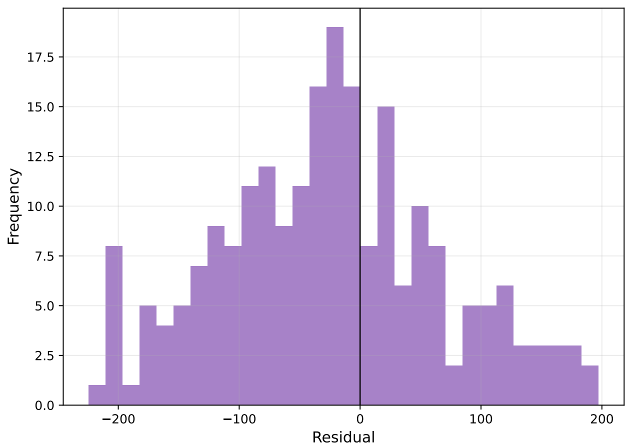

(c) Residual distribution for $A(t)$.

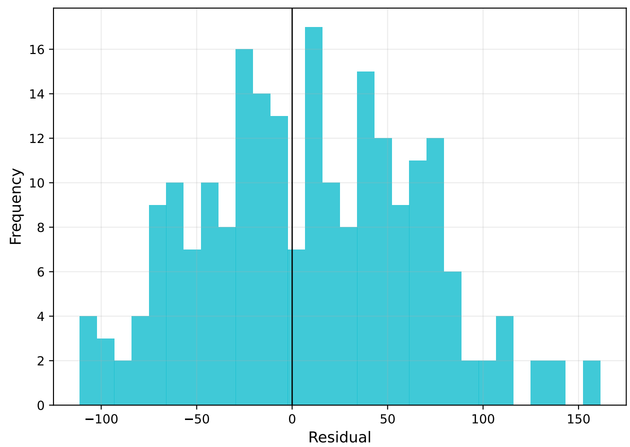

(d) Residual distribution for $T(t)$.

Figure 15. Residual histograms for the reconstructed hidden states.

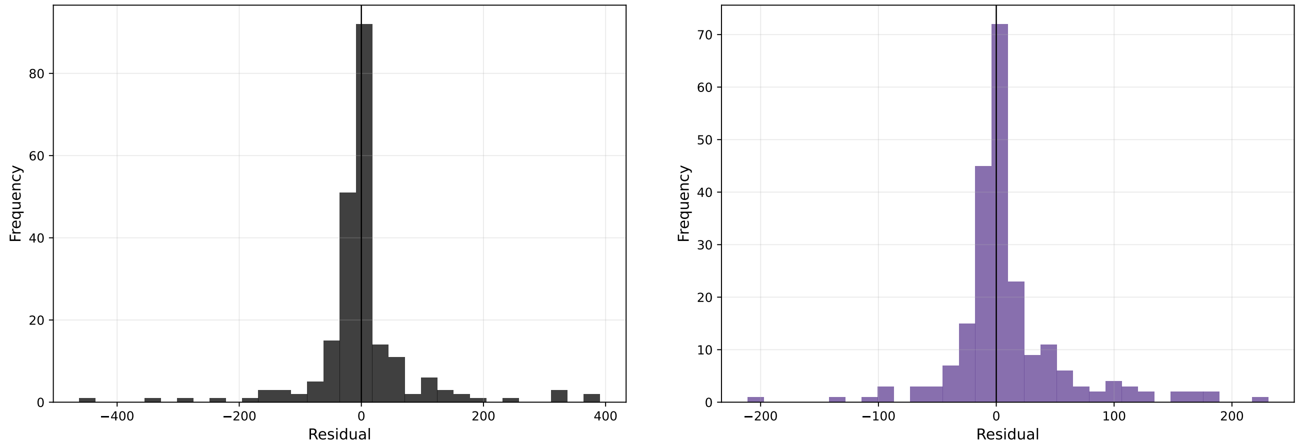

(a) Case-count residual distribution. **(b)** Admission residual distribution.

Figure 16. Residual histograms for the synthetic observation channels.

Normal-probability plots, autocorrelation plots, rolling RMSE curves, and residual-versus-prediction plots are used as complementary diagnostics for distributional shape, lag dependence, local error growth, and systematic bias [27, 28]. These diagnostics are reported in Figures 17–20. The time-dependent diagnostic curves use the normalized computational time scale.

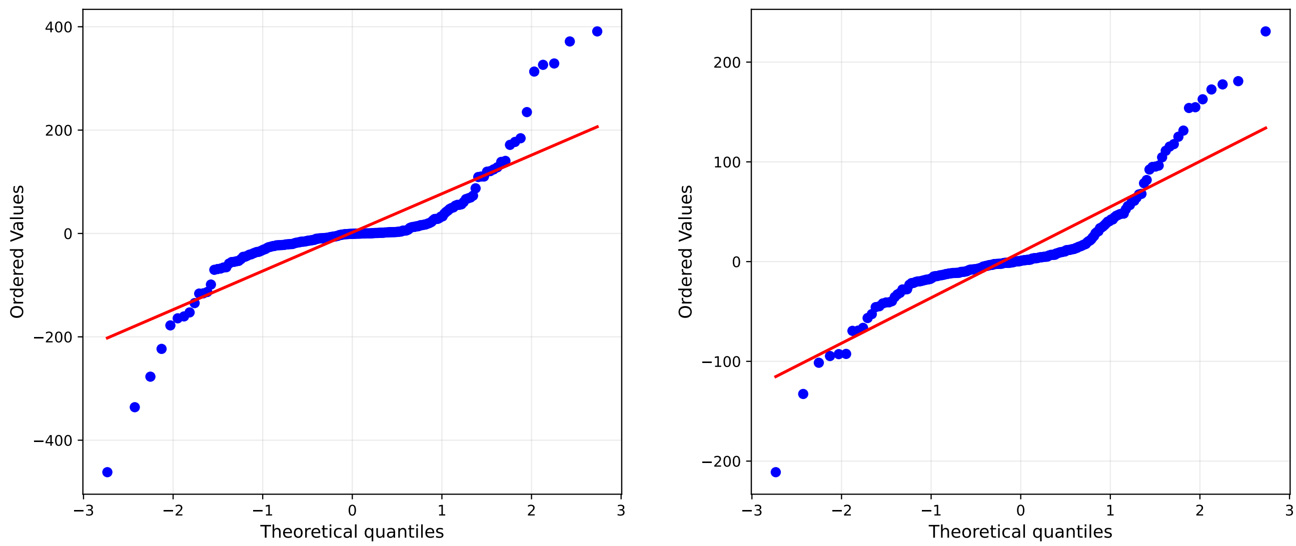

(a) QQ plot for case-count residuals. **(b)** QQ plot for admission residuals.

Figure 17. Normal-probability plots for the observation residuals.

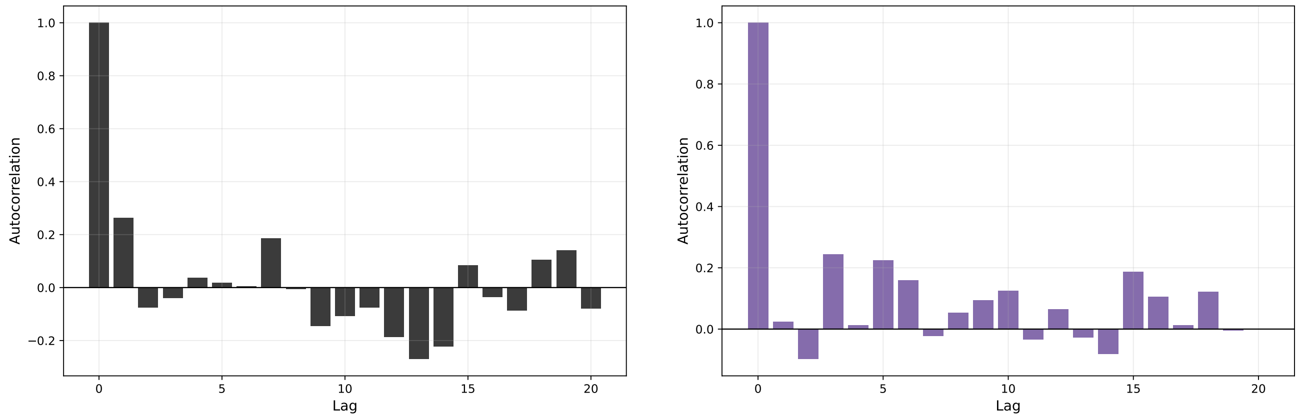

(a) Autocorrelation of case-count residuals.

(b) Autocorrelation of admission residuals.

Figure 18. Autocorrelation diagnostics for the observation residuals.

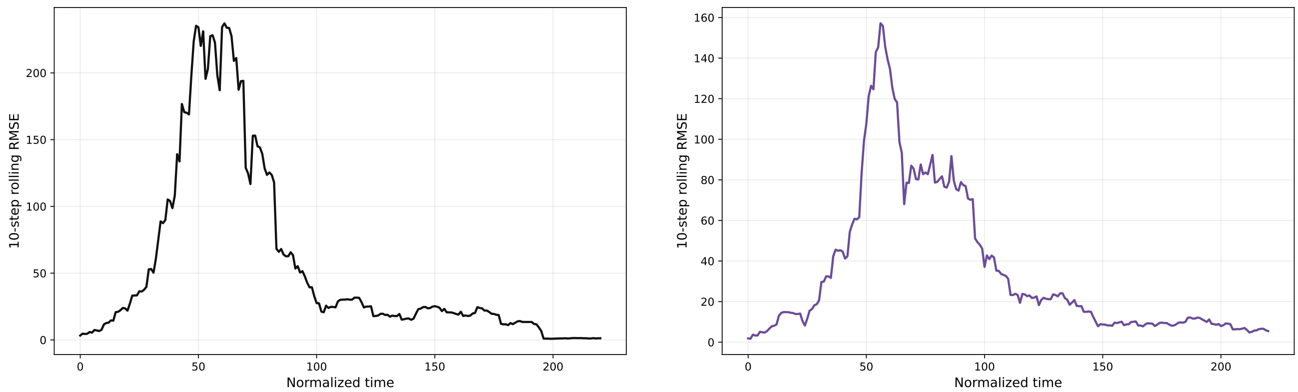

(a) Rolling RMSE for the case-count signal.

(b) Rolling RMSE for admissions.

Figure 19. Ten-step rolling RMSE for the synthetic observation channels.

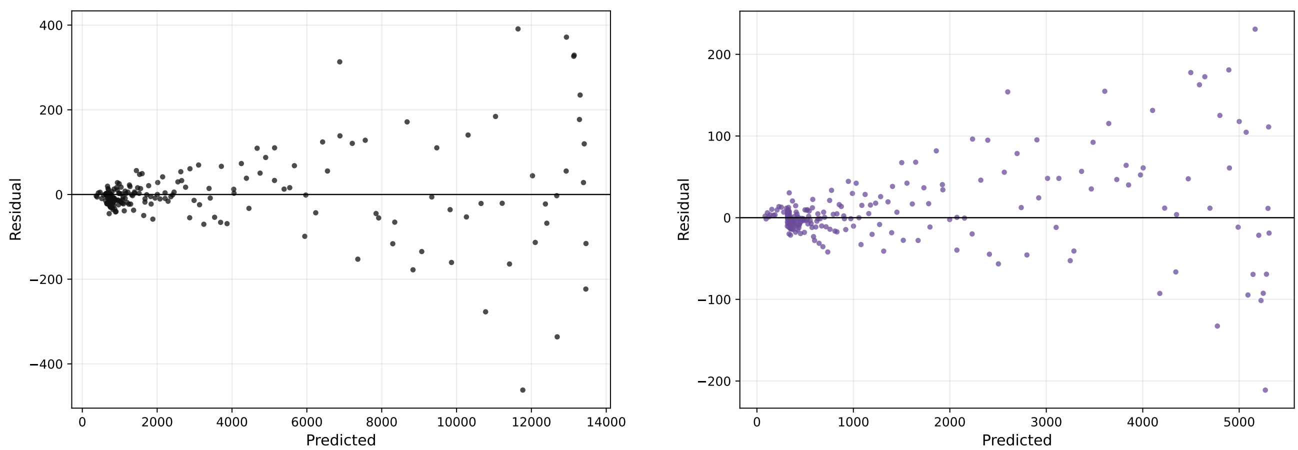

(a) Case-count residuals versus predictions.

(b) Admission residuals versus predictions.

Figure 20. Residuals versus predicted values for the case-count and admission signals.

6.6. Physics consistency

The equation-level consistency is evaluated using the fractional residual already defined in (6.1). The global residual norm is

$$\|\mathcal{R}(t_n)\|_2 = \left(\sum_{j\in\{S,E,I,A,T,R\}} |\mathcal{R}_j^n|^2 \right)^{1/2}.$$

Small values of this quantity indicate that the learned trajectories do not merely fit $C(t)$ and $H(t)$ but also remain compatible with the governing multi-order SEIATR equations. The global and componentwise residual diagnostics are shown in Figure 21.

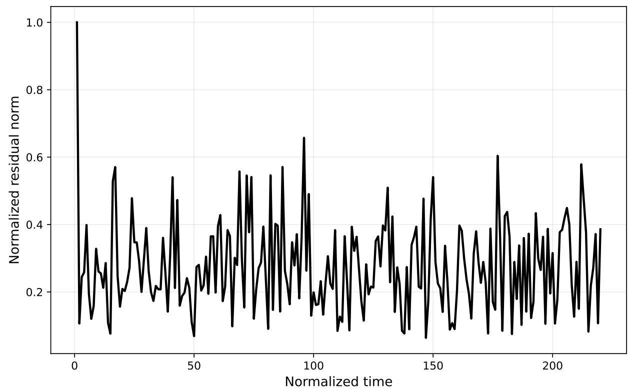

(a) Normalized physics residual norm.

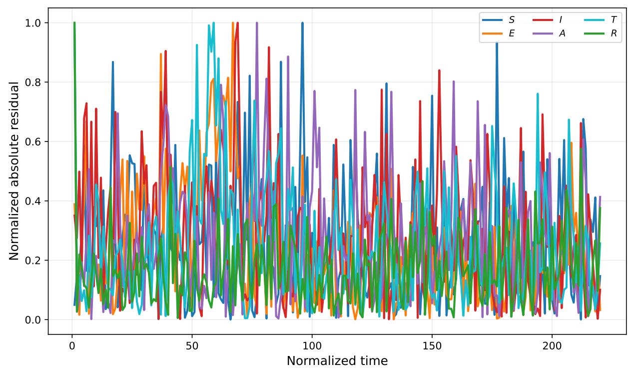

(b) Componentwise physics residuals.

Figure 21. Physics-consistency diagnostics based on the multi-order fractional residual.

6.7. Short-horizon forecasting and model comparison

The learned representation is used for short-horizon forecasting of the synthetic case-count signal over the test window. Forecast horizons of 7, 14, 21, and 30 normalized time steps are considered. The corresponding forecasts are shown in Figure 22. The uncertainty intervals are generated from repeated computational forecast samples around the learned trajectory.

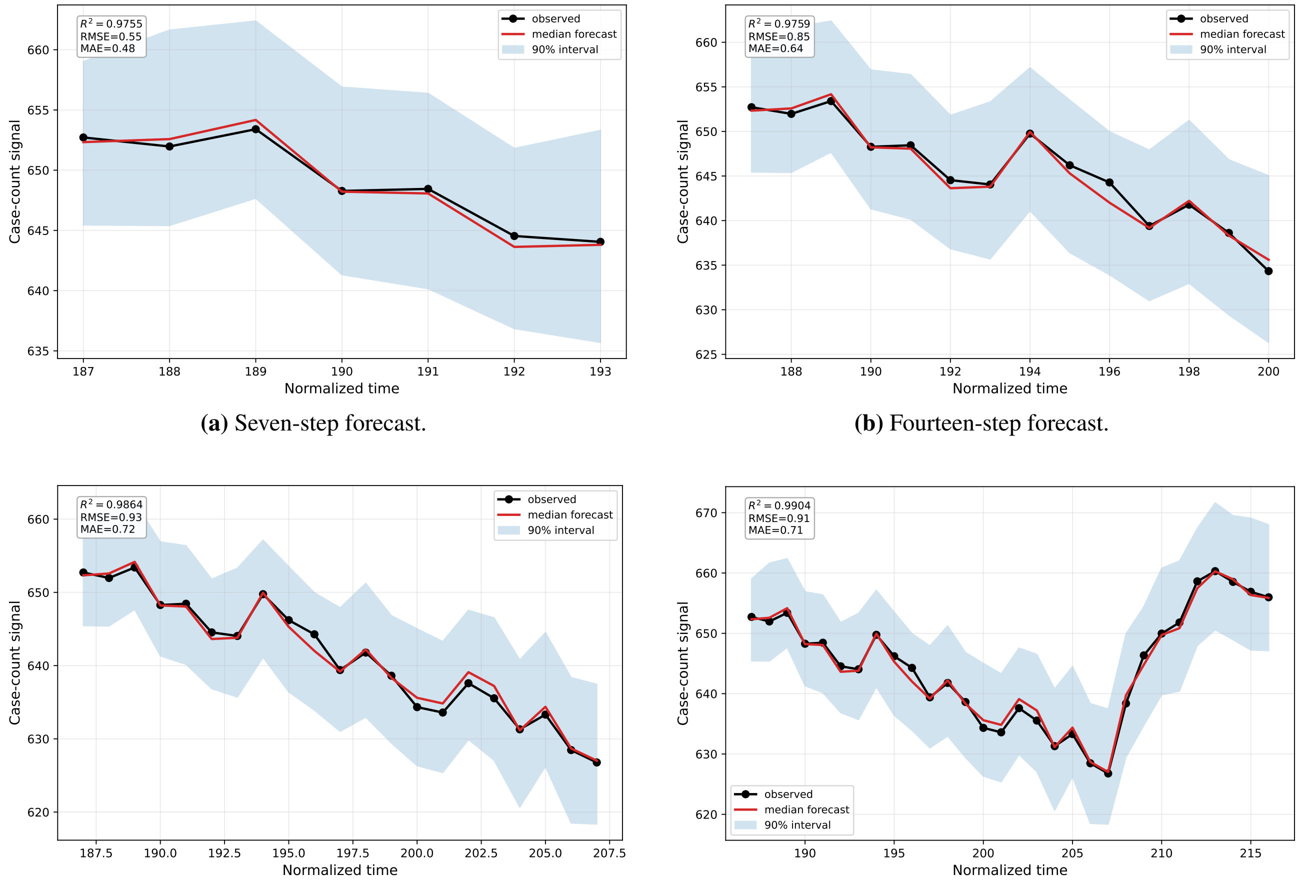

(a) Seven-step forecast.

(b) Fourteen-step forecast.

(c) Twenty-one-step forecast.

(d) Thirty-step forecast.

Figure 22. Short-horizon forecasts of the synthetic case-count signal under the normalized computational time scale.

Figures 23–25 summarize the horizon-specific forecast errors, predictive uncertainty, and interval calibration.

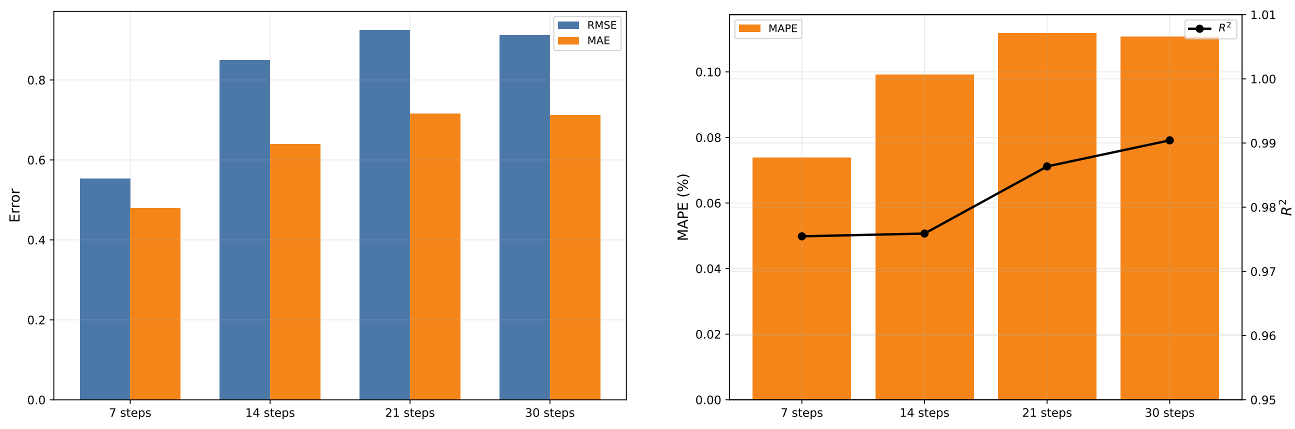

(a) RMSE and MAE by forecast horizon.

(b) MAPE and R^2 by forecast horizon.

Figure 23. Forecast accuracy metrics for the 7-, 14-, 21-, and 30-step horizons.

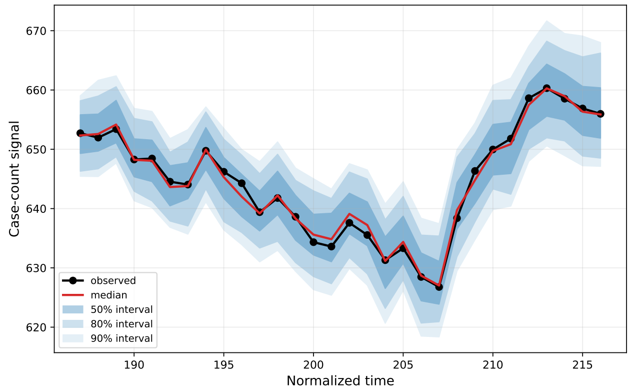

(a) Forecast fan chart.

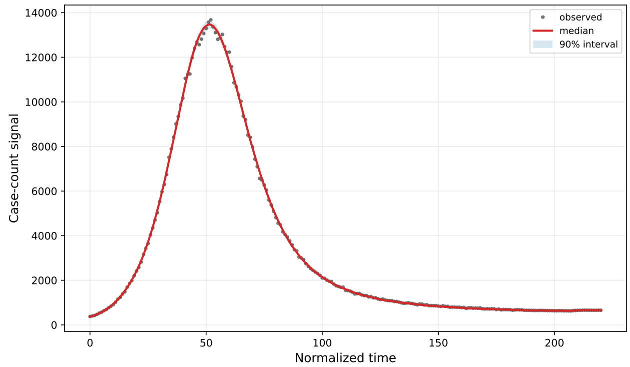

(b) Full-period predictive uncertainty.

Figure 24. Predictive uncertainty diagnostics for the synthetic case-count signal.

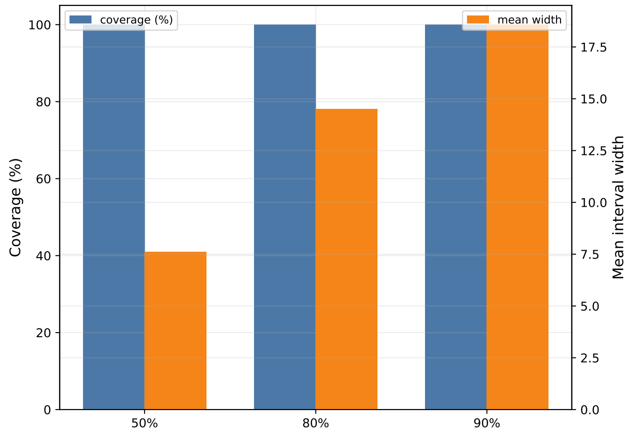

(a) Predictive interval coverage and width.

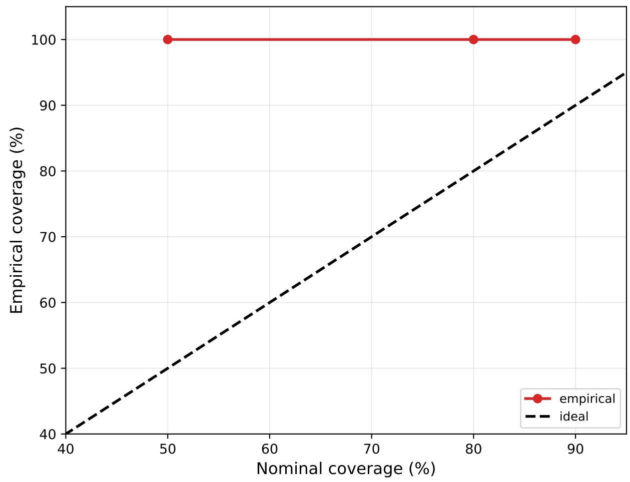

(b) Interval calibration curve.

Figure 25. Calibration diagnostics of the predictive intervals.

For comparison, we include an LSTM-type sequence learner and an ARIMA-type statistical baseline for the same synthetic case-count signal [28, 29]. The computational comparison is shown in Figure 26. This comparison is only a computational benchmark. It is not a claim that the proposed method would necessarily outperform these models on empirical surveillance data, because the proposed PINN is constrained by the same governing equations that generated the reference data.

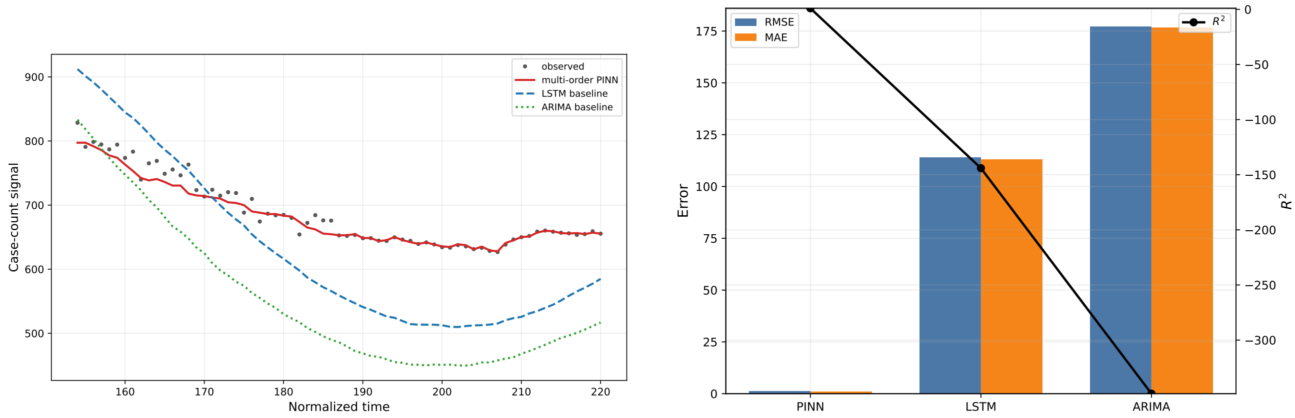

(a) Test-window forecast comparison. **(b)** Comparison metrics.

Figure 26. Computational comparison between the physics-informed multi-order framework and baseline learners.

For the case-count signal, the proposed framework gives RMSE = 86.65, MAPE = 1.28%, and R^2 = 0.999500. The LSTM baseline gives RMSE = 130.25, MAPE = 7.44%, and R^2 = 0.998870, whereas the ARIMA baseline gives RMSE = 165.43, MAPE = 10.72%, and R^2 = 0.998177. These values show lower error for the proposed framework in the controlled synthetic benchmark.

The ablation-style comparison of the full framework and reduced variants is presented in Figure 27.

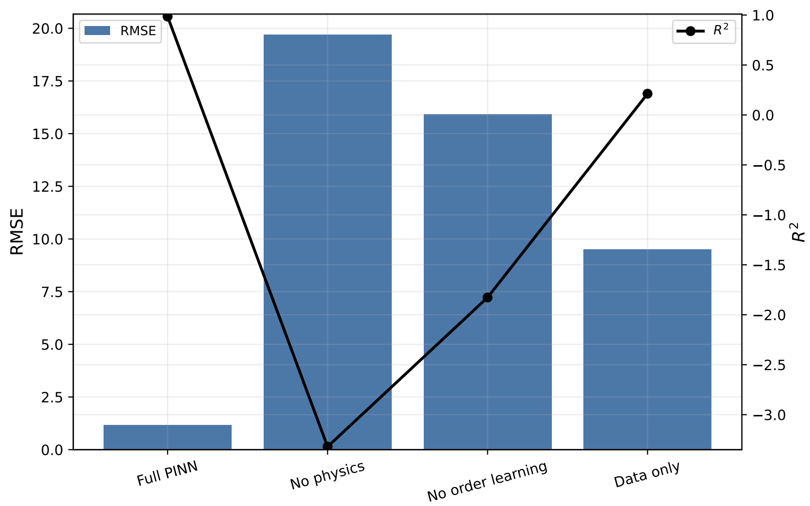

Figure 27. Ablation-style diagnostic comparison between the full physics-informed multi-order framework and reduced variants.

Overall, the physics-informed benchmark shows that the proposed framework can reconstruct hidden states, identify selected epidemiological parameters and fractional orders, maintain consistency with the multi-order residual, and produce short-horizon forecasts in a controlled synthetic setting. The main limitation is that the benchmark is generated from the same equations used in the physics loss. The additional noise-injection test in Table 6 evaluates sensitivity to controlled synthetic perturbations, but it does not replace validation with empirical surveillance data. Robustness under missing observations, reporting delays, time-varying parameters, and model misspecification remains outside the scope of the present benchmark.

7. Key findings and limitations

The proposed incommensurate SEIATR formulation assigns a distinct Caputo order to each compartment. This separates the memory effects of S, E, I, A, T, and R, whereas commensurate models impose a single memory index on the whole system.

The analysis establishes local well-posedness, positivity, boundedness, and biological feasibility. Because the fractional orders are different, boundedness is obtained through componentwise comparison estimates rather than by deriving a single fractional equation for the total population $N(t)$.

The threshold quantity is

$$\mathcal{R}_0 = \frac{\beta\sigma}{\sigma + d}\left(\frac{p_s}{\kappa + r_I + d} + \frac{\theta_A(1 - p_s)}{r_A + d}\right).$$

This quantity depends on the epidemiological rates and does not contain the fractional orders explicitly. The orders affect the transient behavior of the epidemic, especially peak timing, active-burden persistence, and treatment response.

The numerical simulations show that epidemiological parameters mainly control amplification and threshold behavior, while compartment-specific fractional orders mainly regulate timing, broadening, and memory-driven persistence. The physics-informed learning experiment shows accurate reconstruction and parameter recovery within a controlled synthetic benchmark.

The main limitation is that the learning results are generated from the same mathematical model used to constrain the physics-informed learner. Therefore, the reported high reconstruction and forecasting accuracy should be interpreted as a self-consistency benchmark, not as empirical surveillance validation. The added noisy-observation stress test improves the numerical assessment, but broader tests with structured noise, missing data, time-varying parameters, model mismatch, and real surveillance records are required before operational use.

8. Conclusions and future work

This study introduced an incommensurate fractional SEIATR model with distinct Caputo orders $\nu_S, \nu_E, \nu_I, \nu_A, \nu_T$, and ν_R. The proposed model was shown to be locally well posed, positive, bounded, and biologically feasible. The disease-free and endemic equilibria were derived, and the basic reproduction number was obtained using the next-generation matrix approach.

The stability analysis was formulated within the rational-order incommensurate Caputo framework using the corresponding characteristic equation. The numerical simulations indicated that compartment-specific memory modifies the timing, persistence, and shape of the epidemic wave, while the epidemiological rates determine the threshold and amplification mechanisms.

The physics-informed learning framework was used as a controlled computational benchmark for hidden-state reconstruction, parameter estimation, fractional-order identification, residual diagnostics, and short-horizon forecasting. The comparison with data-driven baselines should be understood in this benchmark setting, since the proposed method explicitly uses the governing equations whereas purely statistical baselines do not.

Future work will focus on empirical data calibration, noisy and partially observed data, time-varying transmission, vaccination and intervention effects, stochastic perturbations, alternative fractional operators, and more extensive comparisons with different learning architectures.

Author contributions

All authors contributed equally to the conceptualization, methodology, formal analysis, numerical simulations, validation, investigation, writing–original draft, writing–review and editing, and final approval of the manuscript.

Use of Generative-AI tools declaration

The authors declare they have not used Artificial Intelligence (AI) tools in the creation of this article.

Acknowledgments

Princess Nourah bint Abdulrahman University Researchers Supporting Project number (PNURSP2026R831), Princess Nourah bint Abdulrahman University, Riyadh, Saudi Arabia.

The authors extend their appreciation to the Deanship of Scientific Research at Northern Border University, Arar, KSA for funding this research work through the project number “NBU-FPEJ-2026-2443-05”.

Conflict of interest

The authors declare that they have no conflict of interest.

References

1. H. W. Hethcote, The mathematics of infectious diseases, *SIAM Rev.*, **42** (2000), 599–653. http://dx.doi.org/10.1137/S0036144500371907
2. M. Martcheva, *An introduction to mathematical epidemiology*, Springer: New York, NY, USA, 2015.
3. I. Podlubny, *Fractional differential equations*, Academic Press: San Diego, CA, USA, 1999.
4. K. Diethelm, *The analysis of fractional differential equations*, Springer: Berlin/Heidelberg, Germany, 2010.
5. A. A. Kilbas, H. M. Srivastava, J. J. Trujillo, *Theory and applications of fractional differential equations*, Elsevier: Amsterdam, The Netherlands, 2006.
6. N. Debbouche, A. Ouannas, I. M. Batiha, G. Grassi, Chaotic dynamics in a novel COVID-19 pandemic model described by commensurate and incommensurate fractional-order derivatives, *Nonlinear Dynam.*, **109** (2022), 33–45. http://dx.doi.org/10.1007/s11071-022-07416-6
7. N. Debbouche, A. Ouannas, I. M. Batiha, G. Grassi, M. K. A. Kaabar, A. O. Almatroud, Chaotic behavior analysis of a new incommensurate fractional-order Hopfield neural network system, *Complexity*, **2021** (2021), 3394666. https://doi.org/10.1155/2021/3394666

8. M. A. Hammad, R. Alkhateeb, G. Farraj, N. Djenina, A. Ouannas, Discrete fractional incommensurate order Ebola model: Analyzing dynamics and numerical simulation, *Fractals*, **33** (2025), 2540127. http://dx.doi.org/10.1142/S0218348X2540127X

9. A. Aloui, A. Hioual, O. Kahouli, S. Albadran, M. Ksantini, M. B. Amara, et al., The fractional SI reaction–diffusion model with incommensurate orders: Stability analysis and numerical simulations, *Fractal Fract.*, **10** (2026), 3. https://doi.org/10.3390/fractalfract10010003

10. O. Kahouli, I. Zouak, S. Almohaimeed, A. Ouannas, Y. Bahou, I. Abidi, et al., Chaos and complexity in a fractional discrete memristor based on a computer virus model, *Fractal Fract.*, **10** (2026), 229. https://doi.org/10.3390/fractalfract10040229

11. E. Solouma, M. Alsulami, H. M. Baskonus, A. F. Aljohani, S. Saber, On the stochastic simulation by optimal control and bifurcation analysis of the computer virus model in Caputo-type, *Alex. Eng. J.*, **144** (2026), 12–22. http://dx.doi.org/10.1016/j.aej.2026.04.017

12. A. Boukabache, Stability analysis of a COVID-19 SIR model with direct and indirect transmission, *Nonlinear Dynam. Syst. Theor.*, **25** (2025), 386–398.

13. N. E. Alsubaie, F. El Guma, K. Boulehmi, N. Al-Kuleab, M. A. Abdoon, Improving influenza epidemiological models under Caputo fractional-order calculus, *Symmetry*, **16** (2024), 929. http://dx.doi.org/10.3390/sym16070929

14. S. A. Alharbi, M. A. Abdoon, R. Saadeh, R. D. Alsemiry, R. Allogmany, M. Berir, et al., Modeling and analysis of visceral leishmaniasis dynamics using fractional-order operators: A comparative study, *Math. Method. Appl. Sci.*, **47** (2024), 9918–9937. http://dx.doi.org/10.1002/mma.10101

15. F. El Guma, M. A. Abdoon, S. J. M. Abdalla, S. A. Alharbi, R. D. Alsemiry, R. Allogmany, et al., Fractional-order modeling of influenza dynamics: Impact of memory effect and severity-based variations, *Int. J. Biomath.*, 2025, 2550127. http://dx.doi.org/10.1142/S179352452550127X

16. N. Almutairi, S. Saber, Application of a time-fractal fractional derivative with a power-law kernel to the Burke–Shaw system based on Newton's interpolation polynomials, *MethodsX*, **12** (2024), 102510. http://dx.doi.org/10.1016/j.mex.2023.102510

17. F. M. K. Almalki, E. Solouma, M. Yavuz, S. Saber, A. Sarrah, Analytical and numerical study of bifurcations and reaction-diffusion patterns in a predator-prey model with Holling-III response and variable carrying capacity, *Ain Shams Eng. J.*, **17** (2026), 104131. http://dx.doi.org/10.1016/j.asej.2026.104131

18. N. Raza, A. Bakar, A. Khan, C. Tunç, Numerical simulations of the fractional-order SIQ mathematical model of corona virus disease using the nonstandard finite difference scheme, *Malays. J. Math. Sci.*, **16** (2022), 391–411. http://dx.doi.org/10.47836/mjms.16.3.01

19. D. Matignon, *Stability results for fractional differential equations with applications to control processing*, In: Proceedings of the IMACS-SMC, Lille, France, 1996, 963–968.

20. N. Djenina, A. Ouannas, S. Momani, G. Grassi, *Stability investigation of nonlinear fractional difference equations with incommensurate orders*, In: Fractional Calculus and Applications, Springer Proceedings in Mathematics & Statistics, Springer: Cham, Switzerland, 2025, 171–182. https://doi.org/10.1007/978-3-031-95381-1_10

21. M. Raissi, P. Perdikaris, G. E. Karniadakis, Physics-informed neural networks: A deep learning framework for solving forward and inverse problems involving nonlinear partial differential equations, *J. Comput. Phys.*, **378** (2019), 686–707. http://dx.doi.org/10.1016/j.jcp.2018.10.045

22. G. E. Karniadakis, I. G. Kevrekidis, L. Lu, P. Perdikaris, S. Wang, L. Yang, Physics-informed machine learning, *Nature Rev. Phys.*, **3** (2021), 422–440. http://dx.doi.org/10.1038/s42254-021-00314-5

23. S. Cuomo, V. S. Di Cola, F. Giampaolo, G. Rozza, M. Raissi, F. Piccialli, Scientific machine learning through physics-informed neural networks: Where we are and what is next, *J. Sci. Comput.*, **92** (2022), 88. http://dx.doi.org/10.1007/s10915-022-01939-z

24. V. Lakshmikantham, A. S. Vatsala, Basic theory of fractional differential equations, *Nonlinear Analy.-Theor.*, **69** (2008), 2677–2682. http://dx.doi.org/10.1016/j.na.2007.08.042

25. P. van den Driessche, J. Watmough, Reproduction numbers and sub-threshold endemic equilibria for compartmental models of disease transmission, *Math. Biosci.*, **180** (2002), 29–48. http://dx.doi.org/10.1016/S0025-5564(02)00108-6

26. R. Garrappa, Numerical solution of fractional differential equations: A survey and a software tutorial, *Mathematics*, **6** (2018), 16. http://dx.doi.org/10.3390/math6020016

27. G. E. P. Box, G. M. Jenkins, G. C. Reinsel, G. M. Ljung, *Time series analysis: Forecasting and control*, 5 Eds., Wiley: Hoboken, NJ, USA, 2015.

28. R. J. Hyndman, G. Athanasopoulos, *Forecasting: Principles and practice*, 3 Eds., OTexts: Melbourne, Australia, 2021.

29. S. Hochreiter, J. Schmidhuber, Long short-term memory, *Neural Comput.*, **9** (1997), 1735–1780. http://dx.doi.org/10.1162/neco.1997.9.8.1735

AIMS Press